ABSTRACT

Title of Thesis:	EFFECT OF ISOTHERMAL AGING ON SAC305 HARMONIC VIBRATION DURABILITY
	Elaine Lin, Master of Science, 2016
Thesis Directed By:	Professor Abhijit Dasgupta, Department of Mechanical Engineering

The effect of isothermal aging on the harmonic vibration durability of Sn3.0Ag0.5Cu solder interconnects is examined. Printed wiring assemblies with daisy-chained leadless chip resistors (LCRs) are aged at 125°C for 0, 100, and 500 hours. These assemblies are instrumented with accelerometers and strain gages to maintain the same harmonic vibration profile in-test, and to characterize PWB behavior. The tested assemblies are excited at their first natural frequencies until LCRs show a resistance increase of 20%. Dynamic finite element models are employed to generate strain transfer functions, which relate board strain levels observed in-test to respective solder strain levels. The transfer functions are based on locally averaged values of strains in critical regions of the solder and in appropriate regions of the PWB. The vibration test data and the solder strains from FEA are used to estimate lower-bound material fatigue curves for SAC305 solder materials, as a function of isothermal pre-aging.

EFFECT OF ISOTHERMAL AGING ON SAC305 HARMONIC VIBRATION DURABILITY

by

Elaine Lin

Thesis submitted to the Faculty of the Graduate School of the
University of Maryland, College Park, in partial fulfillment
of the requirements for the degree of
Master of Science
2016

Advisory Committee:
Professor Abhijit Dasgupta, Chair
Professor Bongtae Han
Dr. Michael Osterman

Dedication

This thesis is dedicated to my parents, who have supported me since day one.

Acknowledgements

Many people helped make this thesis possible.

First and foremost is my advisor, Professor Abhijit Dasgupta (better known in the group as Dr. D). He provided an incredible amount of guidance and support throughout my graduate studies. Dr. D displayed amazing patience, knowledge, wisdom, and spent countless hours on discussions for this study, as well as for my benefit. I really could not have asked for a better advisor.

I extend thanks to Professor Bongtae Han and Dr. Michael Osterman for serving on my thesis committee and providing helpful comments. Additional thanks go to Dr. Osterman for providing the test vehicles used in this study. Thank you to Professor Peter Chung for providing his guidance throughout the application process for access to UMD's supercomputers: deepthought 1 & 2. Thank you to Thomas Payerle and David Eisner for their expertise in getting the Abaqus software up and running on deepthought.

Finally, huge thanks go to members of the A-Team, some past and some present, for providing their invaluable advice and help, and the occasional laughs. Many students outside the group helped me out as well, especially Deng, Hannes, Gio, and Sandeep. You all are awesome.

Table of Contents

List of Figures

List of Tables

List of Equations

1 Introduction

Solder joints provide electrical, thermal, and mechanical, interconnections between metallization on PCBs and electronic packages and devices. These joints see a variety of environmental loads throughout their useful life, including vibration and extended exposure to elevated temperatures.

1.1 Lead-free Electronics

Lead-based solder has historically been most prevalent in electronics, being inexpensive with well understood process characteristics and reliability. However in the 2000s, several directives such as RoHS (Restriction of Hazard Substances) and Waste Electrical and Electronic Equipment (WEEE) [1] came about to remove toxic materials such as lead from commercial electronics. The initiative grew in Europe and Japan, then spread worldwide, leading to a transition in the electronics market to lead-free products. While aerospace and military applications have generally been exempt from lead-free compliance so far, the aerospace/defense industry comprises of a small percentage of the total electronics market [2]. Electronics manufacturers often cannot afford to cater to such a small customer base, so even aerospace/defense projects may be compelled to use lead-free electronics in order to utilize modern technologies from a lead-free supply chain.

1.1.1. SAC305

SAC305, a near-eutectic tin-silver-copper alloy (97.5% Sn, 3% Ag, 0.5% Cu), has become a common replacement for SnPb (tin-lead) solders with the onset of RoHS/WEEE. It is particularly popular due to its lower melting temperature (217°C)

compared to other lead-free alternatives, and compatibility with most solder fluxes. Continued durability characterization is needed to understand its reliability under loading conditions relevant to this industry segment.

1.2 Isothermal Aging (Preconditioning)

The electronics industry often practices "preconditioning," or isothermal aging, prior to reliability tests to simulate storage and field use of an electronic assembly. Industry standards such as IPC (Association Connecting Electronics Industries) and JEDEC (Solid State Technology Association) recommend isothermal aging for various reasons. IPC-9701 (Performance Test Methods and Qualification Requirements for Surface Mount Solder Attachments) recommends that board assemblies be "subjected to an accelerated thermal aging (e.g., 24 hours at 100C [212F] {(-0/+5C), (-0/+9F)}) in air to simulate a reasonable use period and to accelerate such possible processes as solder grain growth, intermetallic compound growth, and oxidation" [3]. Isothermal aging is especially a concern for electronics applications in high temperature environments. The mechanical properties and related failure behavior of solder evolve with aging, due to changes in microstructure. It is generally assumed that extended aging decreases the reliability solder joints in vibration, thermal cycling, and drop/shock loading conditions.

1.3 Vibration Durability

There are limited studies on the vibrational durability of lead-free solders, and even fewer with regards to the effects of aging. Vibration is a low stress, high frequency load, commonly encountered during the life of electronic products,

especially in aerospace, military, and automotive applications. Solder interconnects are susceptible to fatigue failures due to vibration, and their durability is affected by additional factors such as isothermal aging.

1.4 Harmonic versus Random Vibration

The test vehicles in this investigation are excited with narrow-band, harmonic vibration, at the first natural frequency, with constant-amplitude excitation. This excitation profile aids in the extraction of material fatigue curves for SAC305, as the uni-modal, constant amplitude properties of harmonic excitation are simpler to model and post-process. Broadband, random vibration is most representative of electronic system use environments, and is most suitable from a qualification testing standpoint. However, it is very complex to model for the purposes of extracting accurate fatigue S-N curves. Several dynamic modes of the test vehicle, as seen in Figure 2, participate under broadband excitation. The strain spectral density plot in Figure 3 compares modal responses of an assembly under random vibration (excited by a (RS) repetitive shock shaker) and harmonic vibration (excited by an (ED) electrodynamic shaker). There is significant participation of multiple high frequency modes on the RS shaker (blue line), versus participation of just a single mode on the ED shaker (red line). With random vibration, additional efforts must be made to reconcile contributions to board deflection from multiple modes, via filtering, cycle-counting and analysis methods that are sensitive to different strain-rates. This creates additional layers of uncertainty and complexity which are undesirable when determining SAC305 fatigue curves. As a result, harmonic vibration excitation is best suited for this investigation.

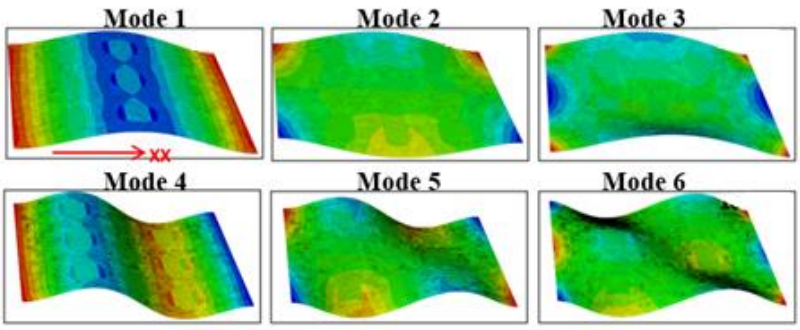

Figure 1: Mode shapes for a rectangular board clamped along short edges, excited in the out-of-board-plane direction

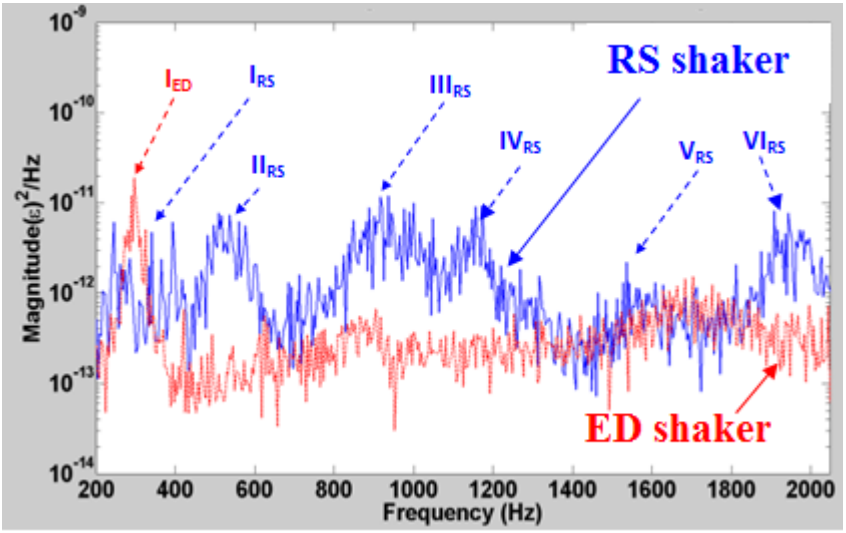

Figure 2: Modal participation in RS (repetitive shock) versus ED (electrodynamic) shakers

1.5 Time Domain Approach

This investigation employs a time-domain approach for the harmonic vibration response analysis. Typically vibration analysis can be done economically in the frequency domain, where signals are segregated into their individual frequency spectra via a Fourier transform. A frequency-domain approach assumes the system dynamic behavior is linear. However, solder material behavior is highly nonlinear (dependent on strain-rate, temperature, aging, etc.). Thus, a time-domain analysis is required, to account for these nonlinearities.

The general procedure of the time-domain approach can be split into three main steps, visualized in Figure 1. The first step is characterization and testing of board assemblies. Boards undergo vibration durability tests at high excitation levels, to experimentally determine the number of cycles to failure of components in the assemblies. Characterization involves recording the PWB strain response, which is used in the next major step—stress analysis via dynamic finite element analysis (FEA). Globally the FEA model of the assembly can approximate the board response in terms of the contribution from the excited mode. At the local level a dynamic simulation of the model estimates SAC solder strains for a given PWB strain, via a strain transfer function. Since strain gages cannot be placed directly onto the solder failure site, the transfer function produced correlates the PWB strain measured in-test to its respective SAC solder strain. Lastly the results from the previous two steps are combined to create material fatigue curves for SAC305.

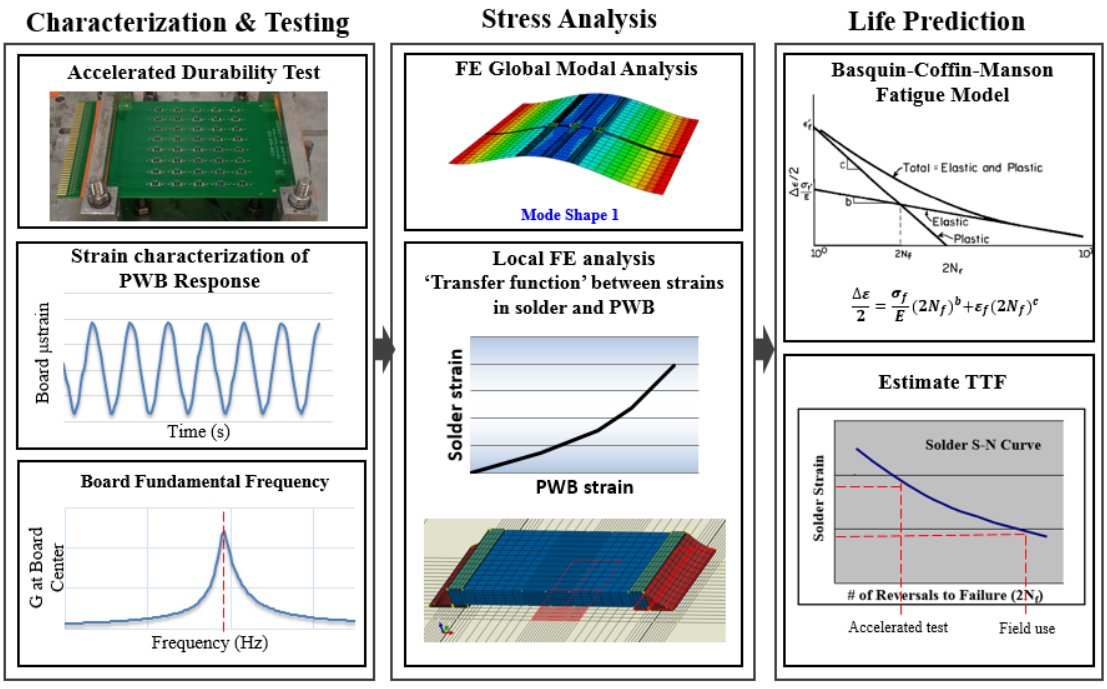

Figure 3: Time-domain approach flowchart

1.6 Problem Statement and Objectives

A primary goal of this study is to obtain material fatigue curves for SAC305 under harmonic vibration excitation, as a function of isothermal aging. This is accomplished with a combination of vibration durability tests and time-domain dynamic FEA. The durability tests provide failure times of components and board response, whereas the dynamic FEA estimates solder response given the in-test board response. This document describes methodology and results to aid in the understanding of isothermal aging effects on harmonic vibration durability of SAC305 interconnects.

2 Literature Review

Solder interconnects are susceptible to fatigue failures due to vibration, and their durability is affected by additional factors such as isothermal aging. The literature has extensively reviewed microstructural change, thermal cycling effects, and stress-strain behavior in SAC305 solder with respect to aging. However, there is more limited examination of the effects of aging on high strain-rate, cyclic loading, such as vibration, especially with modeling efforts to produce SAC305 material S-N fatigue curves.

2.1 Effect of Isothermal Aging on Mechanical Properties of SAC305

There is extensive material in the literature about the effects of isothermal aging on the mechanical properties of SAC305. Motalab and Suhling tested aged SAC305 bulk specimens and observed changes in stress-strain behavior for low strain rates [4]. Properties such as elastic modulus, yield strength, and ultimate tensile strength all decreased with increased aging durations and temperatures. Many researchers have also studied the effects of aging on creep properties of SAC solders (e.g. [5-8]), but this is not directly relevant to fatigue mechanisms in vibration loading. In terms of durability under the cyclic fatigue and high strain rate conditions of vibration, especially for small joint specimens, microstructural changes due to aging are critical. Many researchers [9-21] have studied the effects of isothermal aging on bulk and interfacial microstructure in SAC solders. Major observations are reviewed below for bulk and interfacial intermetallics (IMCs). Aging plays a large role in IMC evolution since IMC growth is diffusion-governed, and thus dependent on temperature and time.

In SAC solders, nanoscale-microscale Ag_3Sn and Cu_6Sn_5 IMCs form in the bulk. With aging, bulk IMC particles coarsen [9-11], meaning they coalesce into fewer, larger particles and the inter-particle spacing typically increases. Since bulk IMCs act as barriers to dislocation movement and crack propagation, aging reduces the resistance to the accumulation of cyclic plasticity and reduces the obstacles for cracks to propagate through the bulk.

Surrounding metallization, particularly the assembly surface finish, dictates the composition of interfacial IMCs. For the SAC/OSP (Organic Solderability Preservative) metal system, Cu_6Sn_5 and Cu_3Sn IMCs form at the SAC/OSP/Cu interface under extensive aging conditions. In addition to the IMCs mentioned for the SAC/OSP/Cu metal system, a SAC/ENIG (Electroless Nickel, Immersion Gold)/Cu system also forms $AuSn_4$, $(Cu,Ni)_6Sn_5$, $(Cu,Ni)_3Sn_4$ at the SAC/ENIG/Cu interface. The main focus of this study is on the SAC305/OSP/Cu system, but a brief comparison of vibration durability in the SAC305/ENIG/Cu system is also presented in later chapters.

Interfacial IMCs at the copper pads and terminations undergo several changes with aging. Interfacial IMC growth is initially composed of Cu_6Sn_5, which increases in thickness with higher temperatures and longer aging times. The greater contribution of thermal energy at high temperatures overcomes the activation energy needed for inter-diffusion of IMC elements (Cu-Sn for OSP). Additionally, interfacial IMCs are initially wavy, scalloped structures, and become less wavy with increased aging. Many researchers have observed a transition from scalloped to flattened

interfacial SAC-Cu IMCs with increased thermal aging [12-16]. A flatter IMC means that less energy is required for cracks to propagate, due to fewer scalloped obstacles.

Extended aging at elevated temperatures (> 100°C) also introduces a second layer of copper rich Cu_3Sn IMCs [9, 12, 13, 17]. As surface area for diffusion decreases with the transition from scalloped to flat tin-rich Cu_6Sn_5 IMCs, and as the Cu_6Sn_5 layer becomes thicker, Sn diffusion to the Cu interface is impeded so a copper-rich Cu_3Sn IMC forms instead. The higher the aging temperature, the less time required to develop this second IMC layer. Rao did not observe a Cu_3Sn layer in 125°C aging of SAC/OSP/Cu interfaces until 500 hours had passed, versus 200 hours at 150°C [12]. This observation is corroborated in this study for 125°C aging, in Chapter 3.3.1. The interface between the two layers is brittle [17-19], which is conducive to fracture under the high strain-rate, cyclic bending loads of vibration. It was also observed that SAC/ENIG/Cu IMCs grew much more slowly than SAC/OSP/Cu IMCs. The $(Cu,Ni)_6Sn_5$ and $(Cu,Ni)_3Sn_4$ IMCs acted as a diffusion barrier to prevent the growth of a Cu_3Sn layer. Researchers have also observed that with extended aging at elevated temperatures, an additional layer of $AuSn_4$ IMCs grows at the SAC/ENIG/Cu interface. The interface between the $AuSn_4$ and initial interfacial IMC layer is brittle [20].

It's important to note that the IMC structure can age even at room temperature. Ma et. al. observed that SAC bulk IMCs visibly coarsened at room temperature during the days after reflow [21]. Many of the data sets discussed in this study come from SAC assemblies which have been stored at room temperature for 2-5 years. As a

result, differences in vibration durability are observed for different room temperature (storage) aging durations, as discussed in subsequent chapters.

2.2 Vibration of Aged SAC305 Solder

Vijayakumar et. al. investigated the effects of long-term moderate-temperature isothermal aging (55°C for 6, 12, and 24 months) on random vibration durability of SAC305 BGA assemblies [22]. An ImAg (Immersion Silver) surface finish was used for all assemblies. Step stress random vibration loads with step increments 2 G_{RMS} every 60 minutes, at room temperature, were used to bring various BGA packages to failure. Characteristic life was observed to decrease with aging, with more drastic changes in durability for extended aging (24 vs 12 months @ 55°C) versus relatively short term aging (6 months @ 55°C). Failure data were described with Weibull distributions and shape parameters β were consistently greater than 1, indicating classical wearout (vibration fatigue) failures. Vijayakumar performed failure analysis on failed samples and found that solder cracks occurred within the interfacial intermetallics.

Qi et. al. investigated the effects of high temperature isothermal aging on random vibration durability of SAC305 insertion mount PDIP (dual in-line package) assemblies [23]. Two SAC305 assemblies with ImSn (Immersion Tin) surface finish were aged at 125°C for 350 hours and at -55°C for 1000 hours, respectively. These assemblies were subjected to room temperature step-stress random vibration loads of 0.1, 0.2, and 0.3 g^2/Hz, for 6 hours at each level. The assembly aged at high temperature yielded earlier failure times than the assembly aged at low temperature. Microstructure was not investigated in failure analysis, but solder failure sites were

identified at the interface between the pad and the solder. SAC305 assemblies of ImSn, ImAg, ENIG, and OSP surface finishes were identically aged at 125°C for 350 hours. For the same random vibration test profile, durability was recorded to be highest in ImSn, followed by ImAg and ENIG, and lastly OSP.

Zhou and Dasgupta investigated the effects of aging on random vibration durability of SAC305 BGA assemblies, with OSP (organic solderability preservative) surface finish [24]. Assemblies were aged for 100 hours and 350 hours at 125°C, after an unknown duration of room temperature storage. This study found that aging decreased time to failure more significantly at higher strains, and less so at lower strains. In addition, Zhou performed harmonic vibration tests on SAC305-OSP assemblies containing LCRs [25]. These assemblies were aged 100 hours at 125°C, in addition to around 2 years of room temperature storage. A two-dimensional, plane stress, quasi-static finite element model was used to estimate solder strains and create SAC305 S-N fatigue curves. Zhou's results are compared with those of this study, in Chapter 5.

Choi et. al. investigated the effects of harmonic vibration on SAC305 HVQFN72 (Heat-sink Very-thin Quad Flat-pack No-leads, 72 joints) assemblies, with an OSP surface finish [26]. These boards were not aged additionally other than approximately 2 years of room temperature storage. Boards were excited at their first natural frequency, at several excitation levels, to produce failures at different stress levels. A three-dimensional, quasi-static finite element model was used to estimate solder strains and create SAC305 S-N fatigue curves. Choi's results are compared with the unaged results of the present study, in Chapter 5.

Paquette and Barker investigated the harmonic vibration durability of SAC305 LCR assemblies identical to those in this study [27]. The boards had ENIG (Electroless Nickel, Immersion Gold) surface finish, and underwent less than 1 year of room temperature storage. Boards were excited at their natural frequency for several excitation levels (110 and 130 G, measured at the board center) to produce failures at different stress levels. No finite element model was developed in Paquette's work, but the finite element model created for the present study can be used to estimate SAC strains in Paquette's work since the test vehicles in both studies are identical. Paquette's results are compared in Chapter 5, with results of the present study, for assemblies with an ENIG surface finish.

Menon et. al. investigated the effects of various surface finishes on harmonic vibration durability of lead-free assemblies [28]. SAC305 BGA assemblies were aged at 100°C for 24 hours and 500 hours. Both ImAg (Immersion Silver) and ENEPIG (Electroless Nickel / Electroless Palladium / Immersion Gold) surface finishes were tested. The same harmonic vibration profile was applied to all boards, at room temperature. Characteristic life was observed to decrease with aging most of the time, and the severity of the decrease varied by surface finish. The noble plating (ENEPIG) showed a drop in vibration durability with isothermal aging, whereas the non-noble plating (ImAg) did not show a statistically significant degradation in durability. It is surmised that the effect of palladium on interfacial IMCs and bulk solder microstructure may have caused the difference. Failure analysis was performed on failed specimens, and mostly solder cracks near the component side of the solder balls were observed. When Weibull distributions were fit to failure data, the shape

parameter β was < 1 for most cases, indicating failures with decreasing failure rates rather than wearout failures. There was speculation that this could have been the result of wide variation in the assembly quality of the test specimens and raises some caveats about the utility of this data for assessing fatigue properties.

The next two studies, by Matkowski et. al. [29] and Pan et. al. [30], involve combined loading conditions (vibration and thermal cycling, and vibration and drop testing, respectively) of aged SAC assemblies. While their insights in failure analysis may be relevant, it is important to note that this study is limited to aging and vibration, not aging and combined loads.

Matkowski et. al. investigated effects of combined thermal cycling and random vibration on SAC305 resistor assemblies with HASL, ENIG, and ImSn surface finishes, aged for 0 hours, 300, and 600 hours at 150°C [29]. Each thermal cycle was 180 minutes long, ranging from -30°C to 120°C. Random vibration excitation consisted of a white noise frequency bandwidth of 50-500Hz, with PSDs of 0.14 g^2/Hz and 2g^2/Hz at the fixture and board center, respectively. The addition of thermal cycling in addition to random vibration produces a very complex thermomechanical loading condition. Failure times, sites, and mechanisms may differ from those of solely-vibration tests of aged components, but insights relevant to vibration of aged SAC305 may still be found in the failure analysis. Matkowski found that the interactions between solder, surface finish, and aging time all affected the reliability of lead-free joints. From experiments, SAC/HASL was more reliable than SAC/ENIG and SAC/ImSn. Matkowski deduced that the thickness and brittleness of

IMC layers were the primary reasons for differences in failure times. IMC layers that were thicker were more susceptible to fatigue.

Pan et. al. studied the effect of gold content in ENIG surface finish on the mechanical durability of various SAC305 assemblies (including QFN5 and QFN6 components), aged for 125°C for 0, 30, and 56 days [30]. The mechanical durability tests consisted of both random vibration and drop testing, performed in succession for several cycles. Random vibration with a PSD of 0.002868 g^2/Hz and bandwidth of 5 – 120 Hz (with the board fundamental frequency at 60 Hz) was applied for 50 minutes. Then, drop testing at 250G with 2.4ms duration was performed for 10 drops. This sequence was repeated 10 times until 500 minutes of vibration and 100 drops were completed. Due to sequential loading condition, vibration durability information is obfuscated, but microstructural failure analysis still provides relevant insights. Pan observed that gold content affected the development of $AuSn_4$ IMCs (bulk and interfacial) with increased aging. Aged assemblies with low Au ENIG finishes exhibited joint fracture in the solder Sn matrix, at high stress levels. Aged assemblies with high Au ENIG finishes exhibited fractures through the developed $AuSn_4$ IMCs in the bulk and near the solder-metallization interface.

Overall the consensus in the literature is that aging decreases the vibration durability of SAC305 interconnects, although to varying extents, depending on surface finish. Efforts have been made to create material S-N fatigue curves for SAC305 harmonic vibration in the literature [25, 26], but none yet as a function of aging and/or surface finish. This study aims to fill that gap, and results and discussion for such will be presented in later chapters.

2.3 Solder Vibration Fatigue Model

A commonly used fatigue model is the Basquin-Coffin-Manson model. It is a combination of the Basquin [31] high-cycle fatigue model, and the Coffin-Manson [32] [33] low-cycle fatigue model to produce a total strain-life curve; both describing material life with a power law, as seen in Equation 1.

$$\frac{\Delta\boldsymbol{\varepsilon}}{\mathbf{2}} = \frac{\boldsymbol{\sigma_f}}{\boldsymbol{E}}(\mathbf{2}\boldsymbol{N_f})^{\boldsymbol{b}} + \boldsymbol{\varepsilon_f}(\mathbf{2}\boldsymbol{N_f})^{\boldsymbol{c}}$$

Equation 1: Basquin-Coffin-Manson Fatigue Model

$\Delta\boldsymbol{\varepsilon}$ = Cyclic strain range

$\boldsymbol{\sigma_f}$ = Fatigue strength coefficient

$\boldsymbol{\varepsilon_f}$ = Fatigue ductility coefficient

$\mathbf{2}\boldsymbol{N_f}$ = Number of cycles to failure

$\boldsymbol{b}$ = Fatigue strength exponent

$\boldsymbol{c}$ = Fatigue ductility exponent

$\boldsymbol{E}$ = Young's modulus

A general Basquin-Coffin-Manson fatigue curve is pictured below in Figure 4 [33]. This is a strain based model, predicting durability of ductile materials based on the applied cyclic strain range. The Coffin-Manson portion (termed low-cycle fatigue – LCF) of the curve is a result of plastic strain contributions to fatigue damage, while the Basquin portion (termed high-cycle fatigue – HCF) is a result of elastic strain contributions. This fatigue model is commonly used for vibration studies [24-26, 35-37]. Some authors may choose to only use the HCF portion [38], depending on

severity of loading conditions, and/or modify the model based on empirical results [39].

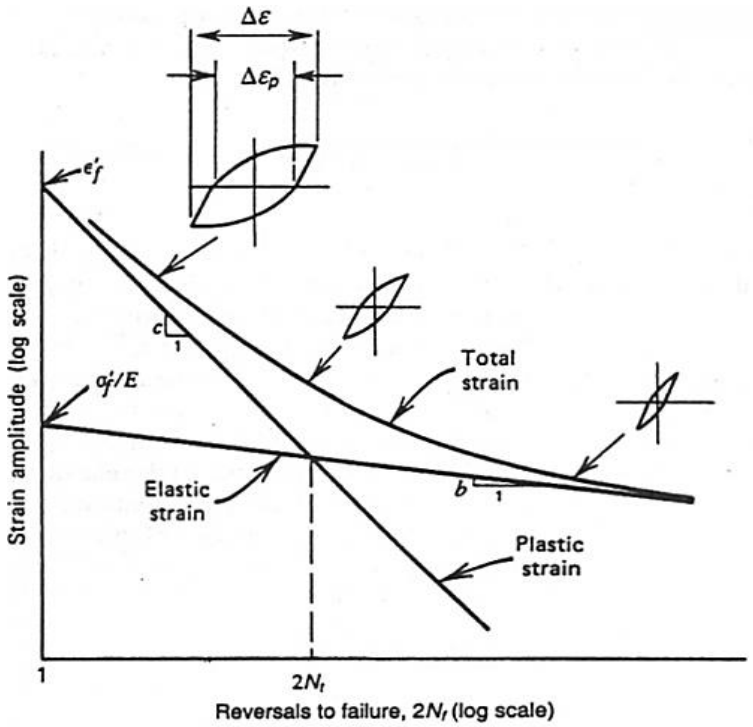

Figure 4: General Basquin-Coffin-Manson Fatigue Curve [34]

2.3.1 Finite Element Modeling Techniques for Vibration Analysis

As explained in Chapter 1.5, solder joints stresses/strains cannot be measured directly during vibration tests, so some modeling efforts are required in order to perform stress analysis to estimate joint strains. Finite element modeling techniques for vibration can be found in the literature for various properties: (i) frequency domain vs. time-domain, and (ii) quasi-static vs. dynamic.

Frequency domain analysis, or modal analysis, only accounts for linear system behavior. Some researchers employ modal analysis to characterize vibration loading effects on solder using linear-elastic solder properties [36, 38, 40-42]. Time-domain

analysis can account for nonlinear system behavior, but greater computational burden is introduced compared to frequency-domain analysis.

Quasi-static models [25, 26, 43] involve imposing static boundary conditions of bending loads seen in vibration, and then estimating solder strains. This method is sometimes preferable due to the smaller computational burden involved, compared to dynamic models. Dynamic models for vibration, which are inherently time-domain analyses, involve applying excitation at the fixed boundaries of the model. This is more representative of vibration loading conditions, and can account for inertial effects. Several researchers have estimated solder stress/strains via dynamic models [35, 44]. While the simulation time is lengthy for dynamic models with high mesh density, it can be reduced with proper application of initial conditions. Further details are discussed in Chapter 4.

3 Experimental Study

Room temperature (~25°C) harmonic vibration tests were first conducted on SAC305 assemblies with OSP (Organic Solderability Preservative) surface finish. Three assemblies were isothermally pre-aged for different lengths of time at 125°C, per Table 1. Previously the boards had been in storage for 5 years, so an extended period of isothermal room temperature aging has also occurred in all the SAC assemblies. The aging temperature of 125°C was chosen since it is a typical peak operating temperature designated by military and aerospace standards.

SAC305-OSP assembly aging conditions
Aged 0 hours @ 125°C + 5 years @ 25°C
Aged 100 hours @ 125°C + 5 years @ 25°C
Aged 500 hours @ 125°C + 5 years @ 25°C

Table 1: Test vehicle aging matrix

Additionally, a SAC305 assembly with ENIG (Electroless Nickel Immersion Gold) surface finish was tested with the same harmonic vibration profile, without any additional aging beyond the 5 years of room temperature storage. As discussed in Chapter 2.1.1, different metal systems resulted in different vibration durability. This data is compared and discussed in Chapters 3-5.

All testing procedures and results are discussed in this chapter.

3.1 Test Setup

An electrodynamic shaker (Figure 5) is used in conjunction with a controller and associated software to provide harmonic excitation.

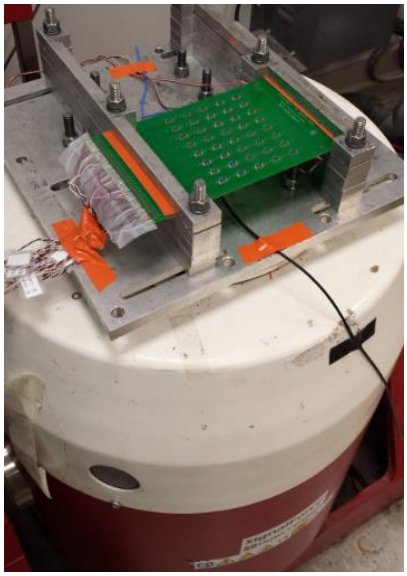

Figure 5: Electrodynamic shaker with fixture and specimen

The test vehicle, pictured in Figure 6, is a 1.6mm thick single-sided FR4 printed wiring assembly (PWA) with an OSP surface finish and copper metallization (pad, traces, thru-holes). An array of forty 2512 leadless chip resistors (LCRs) is organized into 5 columns (Col 1-5 as labeled in Figure 6) and 8 rows. Of these resistors, half are assembled on standard full pads (100% width) and half are assembled on modified narrow pads (20% width), as seen in the upper right inset image in Figure 6. The dimensions of these pads are listed in Table 2.

Each board is clamped along its short edges (as pictured in Figures 5, 6). The middle of the central column (Col 3) resistors lies on the centerline between the clamps. All columns Col 1-5 are equally spaced and symmetric about the Col 3 centerline.

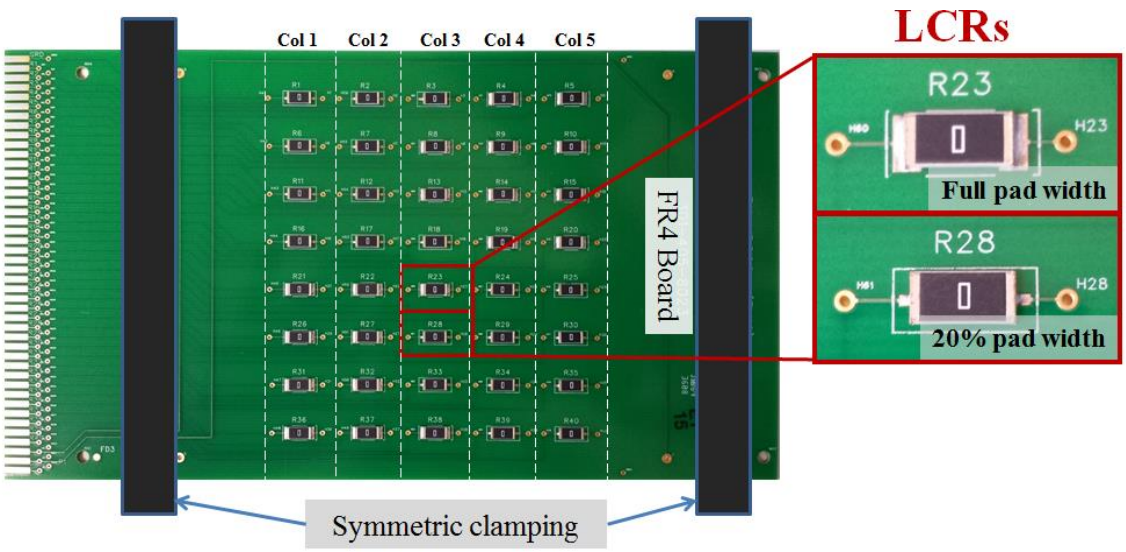

Figure 6: Test vehicle, components, and fixturing

Pad type	Dimensions (mm x mm)
Full (100%) pad	3.3 x 1.65
Narrow (20%) pad	0.66 x 1.65

Table 2: Pad dimensions

These LCRs are daisy-chained for real-time monitoring of failures. A multiplexer is used to monitor the resistances of each resistor, R1 through R40. Directly prior to each test, the initial resistances of all components in the PWA are recorded using a data logger. For all components tested, initial resistances ranged from 1-2 Ohms. Failure is defined as a resistance increase of 20% for 10 consecutive readings of the multiplexer per IPC-9701 standards [2]. The multiplexers collect resistance data approximately every 10 seconds.

The shaker controller is used to monitor and control acceleration at the board center (on the unpopulated side of the PWB). A high sensitivity accelerometer (100 mV/G) is placed on the shaker table, and a lower sensitivity accelerometer (10 mV/G)

is placed at the board center. Figure 7 illustrates the location of the board accelerometer.

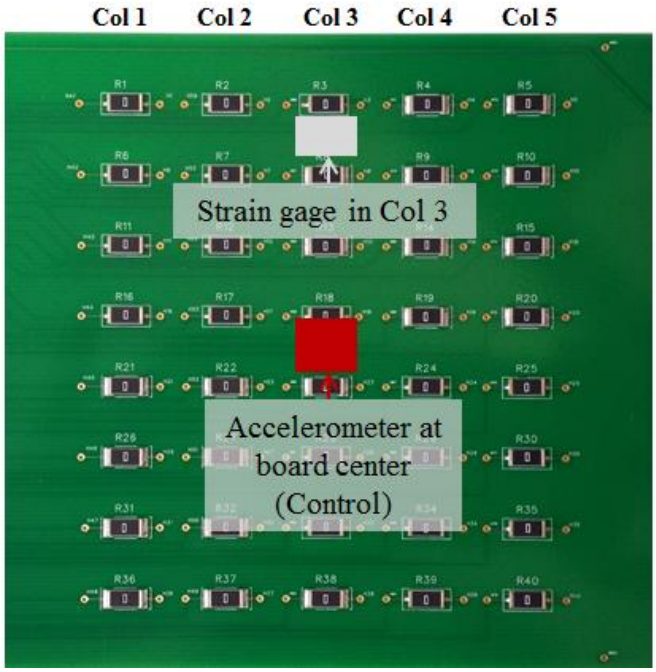

Figure 7: Board instrumentation placement (accelerometer and strain gage placed on unpopulated side)

Test PWAs are excited in the direction normal to the plane of the board, at the board's first fundamental frequency. Prior to each test, the first resonant frequency of the board is determined via a sine sweep, the results of which are presented in Figure 8. A low excitation (0.5G) sine sweep to find the natural frequency. The board natural frequencies ranged from 168 to 178 Hz, with an apparent stiffening of the PWA with isothermal aging (Figure 8). The shaker controller software adjusts to the slight drift in board natural frequency throughout the test and maintains the desired excitation level at the board accelerometer. Since it is unreasonable to test for the entire life cycle of an electronic assembly, the harmonic vibration profile is designed to achieve

failures within a few hours. Excitation at resonance generates large board deflections which accelerate failures on the assemblies.

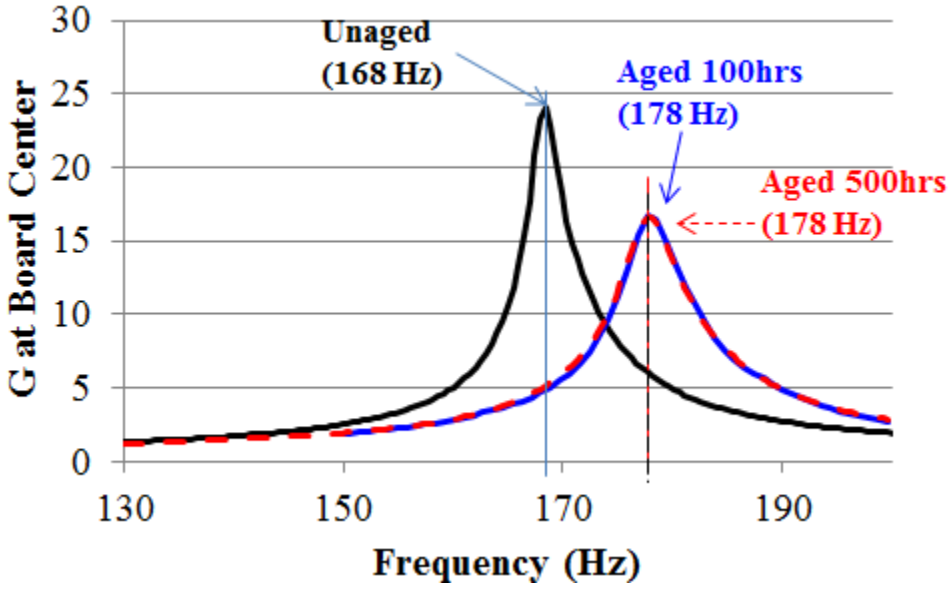

Figure 8: Sine sweep of boards prior to durability tests

3.2 Board Characterization

As illustrated in Figure 7, boards are also instrumented with a strain gage on the unpopulated side of the central column of resistors, to characterize the board response. The gages are oriented along the length of the board, in the direction of principal vibratory board curvature. A data acquisiton unit and associated software are used to record board strain for a short capture period. Strain gages are calibrated in the fixtured assembly, directly prior to each test. Board strains are only measured during the first few minutes of each test. The fatigue degradation of the PWB material causes strain gages to delaminate. Thus only initial strain measurements accurately represent the PWB strain response. Strain data is collected at 5000 Hz for a capture period of one second, in order to monitor board strains through several vibration

cycles. Since the natural frequency of the PWA is approximately 200 Hz, a 5000 Hz capture frequency provides around 25 points per cycle—a sufficient number of points to describe the signal.

The cyclic bending strain range at the central column (Col 3) was measured to be 700 μstrain. Using the curvature information from the FEA modal analysis (described below and also later in Chapter 4), the bending strain range for Cols 2, 4 are estimated to be 580 μstrain.

The first mode shape of this test configuration is as pictured in Figure 9, using preliminary FEA modal analysis. Board curvatures and board strains, and thus corresponding solder strains, are greatest at Col 3 resistors, followed by those at Cols 2, 4, then Cols 1, 5. The board curvature in Cols 1, 5 is found to be too low to induce fatigue failures within a reasonable amount of time. As a result, only components within the central three columns, Cols 2, 3, 4, are considered during durability tests.

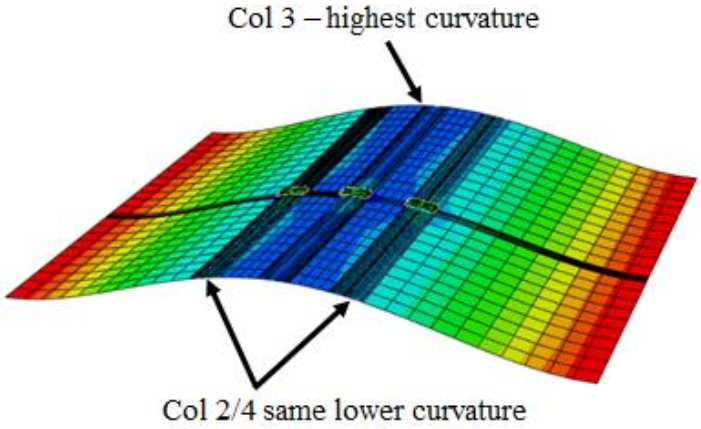

Figure 9: Board curvature for first mode shape

This board configuration allows for four different stress levels, distinguished by pad type and column location. The sample sizes for each stress level are listed in Table 3, sorted from highest to lowest stress. The locations of LCRs in each stress

level grouping in Cols 2, 3, 4 are depicted in Figure 10, corresponding to the color key in Table 3.

Highest stress

Stress Level	Sample Size
20% Col 3	4
20% Col 2/4	8
Full Col 3	4
Full Col 2/4	8

Lowest stress

Table 3: Stress levels and sample sizes

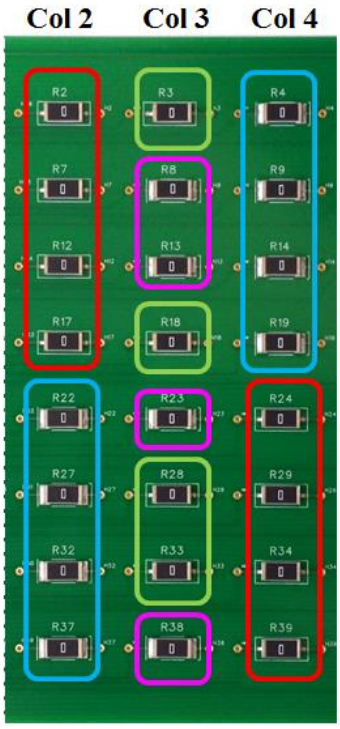

Figure 10: Locations of each stress level grouping (color key in Table 3)

Observing different joint stress levels on a single board allows for more detail on the produced SAC305 material fatigue curve. In addition, the use of LCRs increases the accuracy of FEA outputs, since resistors have relatively simple geometry. Additional uncertainty can be introduced due to model simplification, when modeling more complex components such as BGAs or QFPs.

3.3 Analysis of Failure Data

The statistics of the failure data are captured using 3-parameter Weibull distributions and failure analysis is performed to establish the failure modes, as discussed below in this section.

3.3.1 Failure Analysis

After completion of accelerated durability tests, failure analysis is performed for select components to verify failure modes and identify failure sites. LCR components are cross-sectioned and observed using microscopy via an E-SEM (environmental scanning electron microscope). Early failures were observed to be mostly due to solder cracks (Figure 11), whereas later failures were due to a combination of solder cracks and copper trace cracks (Figure 12). The implications of such are discussed in Chapter 5.2.

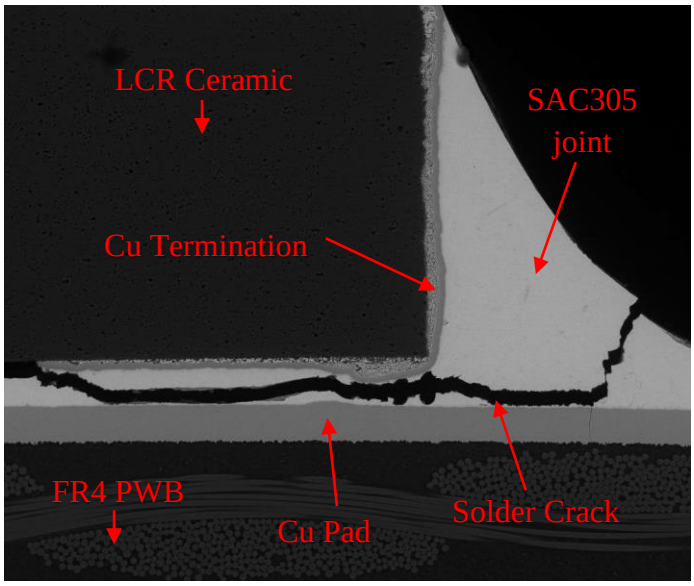

Figure 11: Solder crack failure mode

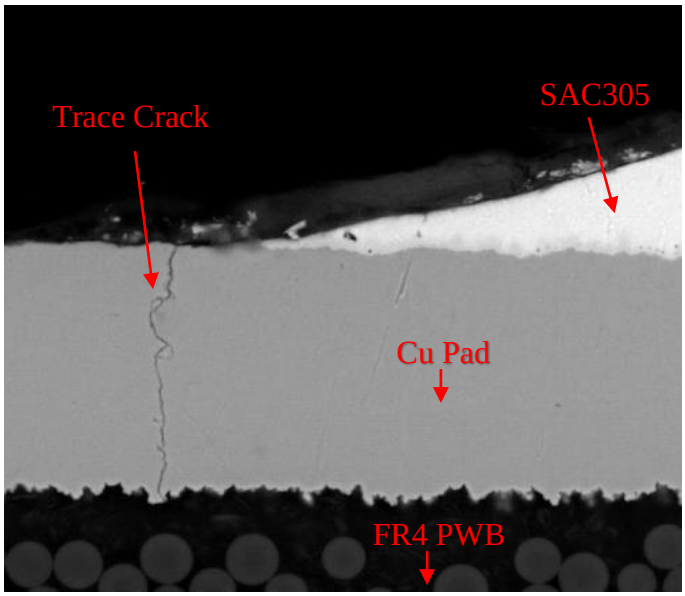

Figure 12: Copper trace crack failure mode

In terms of the effect of aging in influencing these failure modes, possible explanations can be found in joint microstructure, as discussed in Chapter 2. To better observe microstructure, select cross-sections were etched (for specimens aged 0 hours and 500 hours @ 125°C, to bound the answer) with a 2% nital solution for 3 seconds.

Visible coarsening of the bulk intermetallics with aging was observed, which agrees with findings in the literature [9-11], discussed in Chapter 2. Figures 13 and 14 show bulk intermetallics at the same magnification in the aged 0 hours @ 125°C and aged 500 hours @ 125°C specimens, respectively.

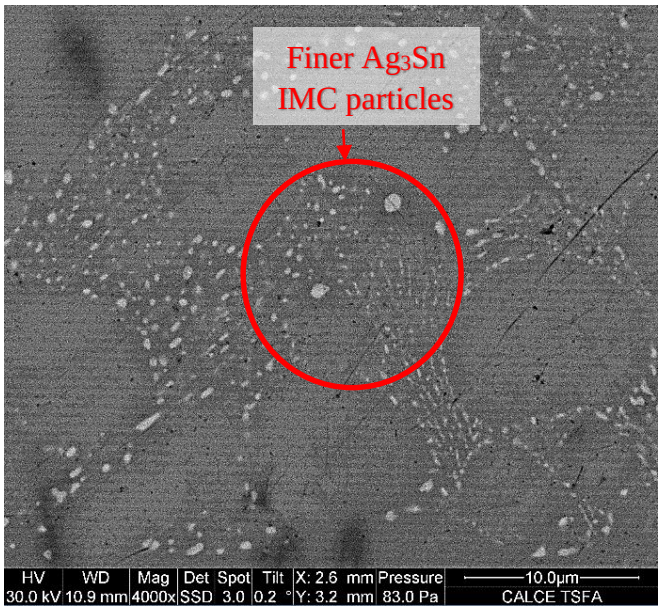

Figure 13: Bulk IMCs (Aged 0 hrs @ 125°C + 5 yrs RT)

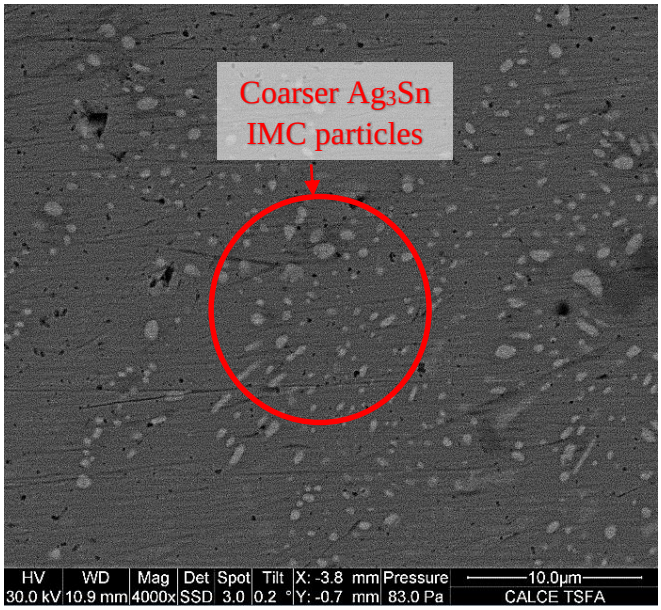

Figure 14: Bulk IMCs (Aged 500 hrs @ 125°C + 5 yrs RT)

Crack propagation is observed along interfacial intermetallics (IMCs) and through the bulk of the solder joints. Figure 15 shows a crack spreading from the interfacial IMC at the copper pad, to the bulk of the solder fillet. Figure 16 shows a crack spreading from the interfacial IMC at the copper termination of the resistor body, to the bulk of the solder fillet.

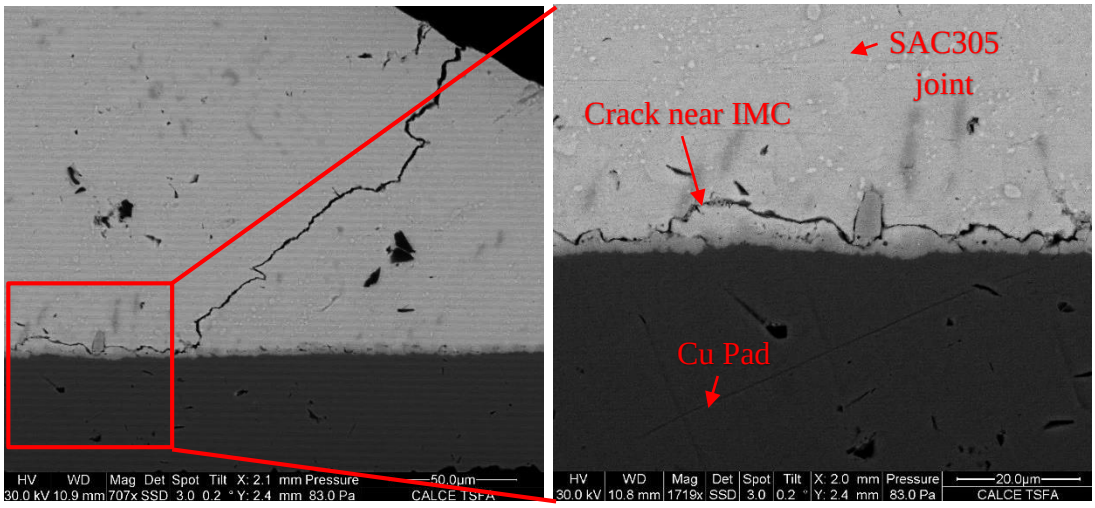

Figure 15: Crack through copper pad interfacial IMC and bulk of solder fillet (Aged 500 hrs @ 125°C + 5 yrs RT)

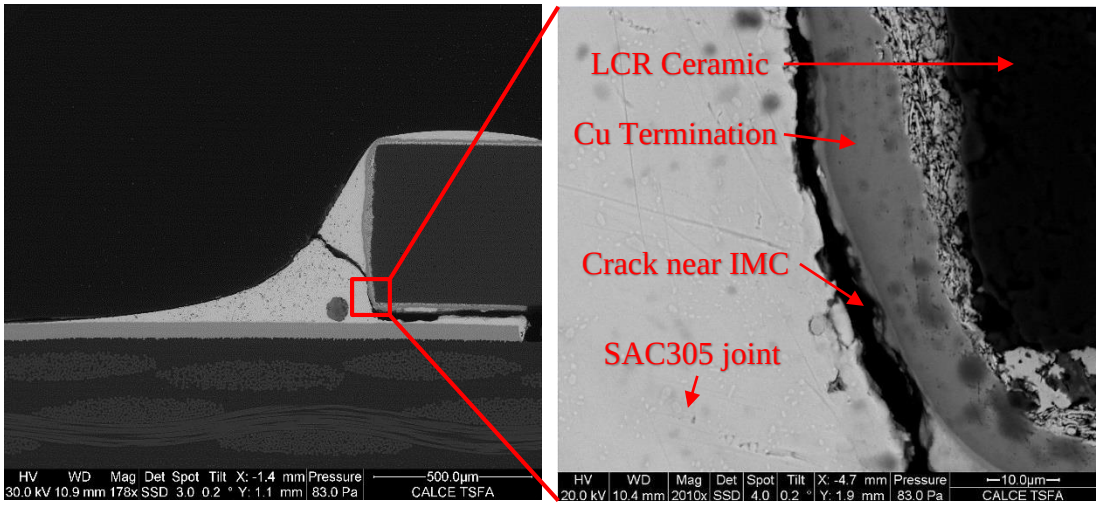

Figure 16: Crack through copper terminal interfacial IMC and bulk of solder fillet (Aged 500 hrs @ 125°C + 5 yrs RT)

Crack propagation may occur more readily with extended aging due to decreased waviness (reduced scallop-like structure) of Sn-rich IMCs. As reviewed in Chapter 2, interfacial IMCs between copper and solder are observed to thicken and weaken with aging. With fewer wavy lobes present, cracks require less energy to propagate. Figures 17-19 demonstrate that waviness of the copper pad interfacial IMCs significantly decreases from 100 hours to 500 hours of aging @ 125°C.

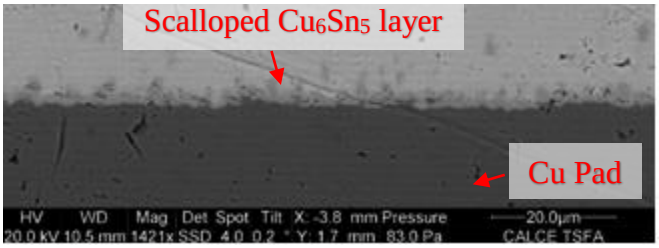

Figure 17: Copper pad interfacial IMC (Aged 0 hrs @ 125°C + 5 yrs RT)

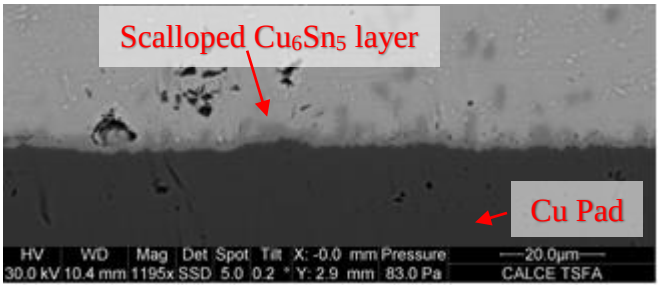

Figure 18: Copper pad interfacial IMC (Aged 100 hrs @ 125°C + 5 yrs RT)

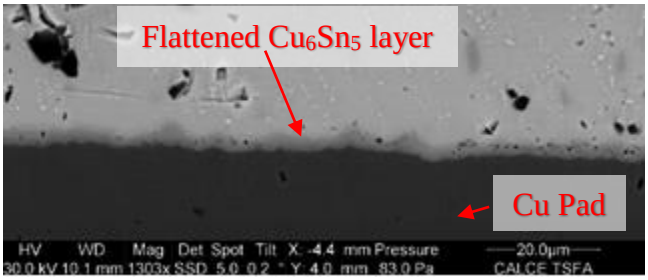

Figure 19: Copper pad interfacial IMC (Aged 500 hrs @ 125°C + 5 yrs RT)

Aging also introduces the growth of a second copper-rich Cu_3Sn IMC layer in addition to the tin-rich Cu_6Sn_5 IMC. The interface between these two layers is brittle

and thus also conducive to crack propagation [17-19]. The two IMC layers are clearly visible in the aged 500 hours @ 125°C specimen, in Figure 20. A Cu-rich IMC layer was not readily observable in the specimens aged for 0 and 100 hours @ 125°C.

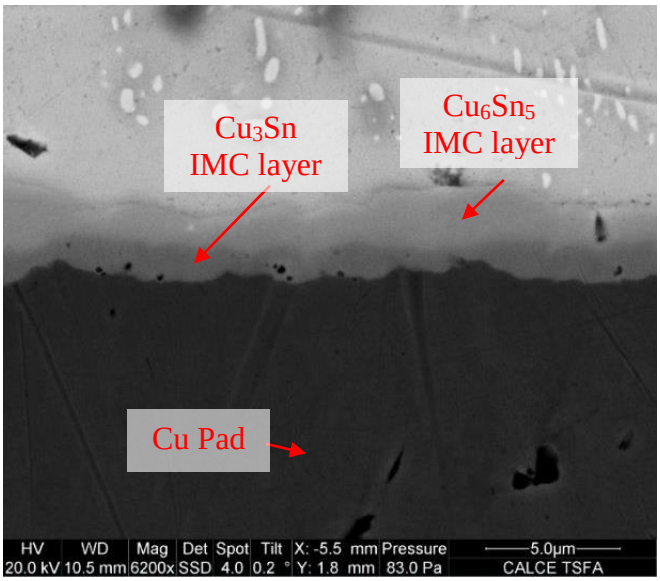

Figure 20: Cu_6Sn_5 and Cu_3Sn interfacial IMC layers at copper pad (Aged 500 hrs @ 125°C + 5 yrs RT)

3.3.2 Weibull Analysis

A three parameter Weibull distribution is fitted to the failure data, shown in Figure 22. Commercial statistical analysis software is used to generate Weibull plots and parameters, using the maximum likelihood estimation (MLE) analysis method. Since each stress level grouping (Table 3) has only a few data points, ratios of characteristic lives (obtained from two-parameter Weibull fits to unscaled data, in Appendix A.3) between groups are used to scale all failure data to the same stress level at each aging condition. In this way, the full population of resistors can be employed for statistical analysis, when assessing the effects of isothermal aging. The data is scaled to the lowest stress level, which is that for full (100% width) pads in

Cols 2, 4. This scaling method assumes that the shape parameter β is the same in distributions across stress levels. To ensure that the scaled β has converged, the β values in Table 4 are enforced on the data to recalculate η for each stress group. The scaling process is repeated with these new η values to confirm that the scaled β remains the same.

Characteristic life is observed to decrease monotonically with aging (Table 4, Figures 21 and 22). The Weibull shape parameter β is around 1.8-1.9 for each aging condition, indicating a wearout failure mode. The Weibull location parameter γ provides an estimate for earliest time a failure is observed. Table 4 shows γ decreases with increased aging, indicating that first-time-to-failures are earlier for longer aging times.

From these data analyses it is clear that increased duration of isothermal aging decreases vibration durability, as observed in previous studies in the literature. Weibull plots and parameters for individual, unscaled stress groupings can be found in Appendix A.3.

Weibull Parameters	Aged 0 Hours	Aged 100 Hours	Aged 500 Hours
β	1.83	1.86	1.88
η	1.05E6	1.01E6	8.55E5
γ	2.79E5	2.57E5	2.16E5
Characteristic Life (η+γ)	**1.33E6**	**1.27E6**	**1.07E6**

Table 4: Weibull distribution fit parameters for aged OSP boards (all data scaled to lowest stress level)

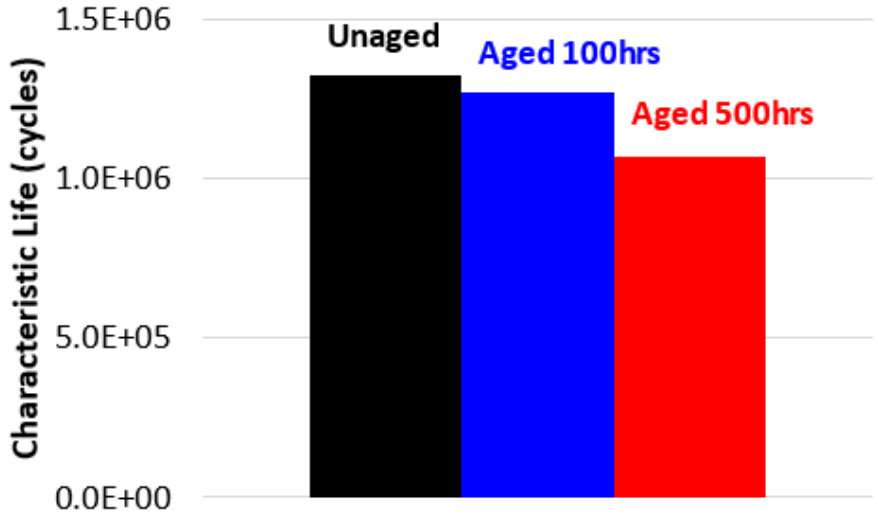

Figure 21: Histogram of characteristic lives for different aging conditions

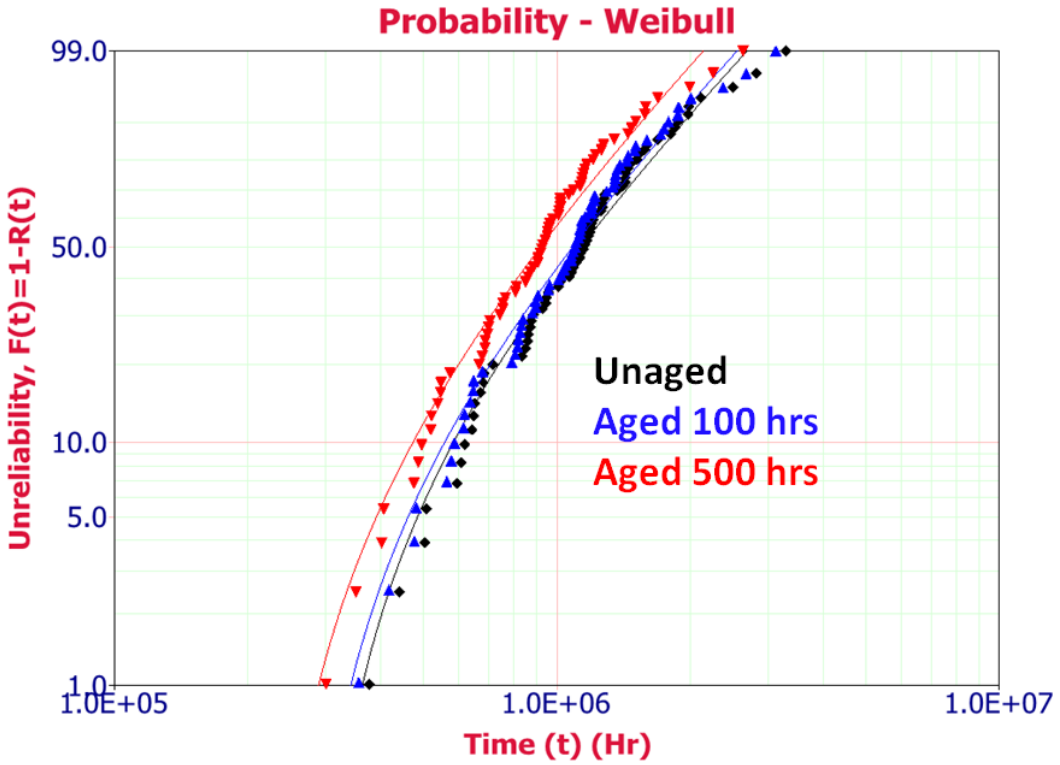

Figure 22: Three parameter Weibull fit to aged OSP board failure data (all data scaled to lowest stress level)

3.4 ENIG Board Testing Results and Analysis

As stated previously, an ENIG PWA of identical configuration to that in Figure 6 underwent a vibration durability test as well. This board was not additionally aged beyond the 5 years of room temperature storage. The same excitation setup is applied: 149G at board center, at the board's natural frequency. The board's initial natural frequency was 180 Hz, and the bending strain range beneath the board was measured to be 700 μstrain (same as the OSP boards). A 3 parameter Weibull distribution is performed to compare with the unaged OSP board. Failure data is scaled to the lowest stress level such that surface finish is the only varying factor. In Figure 23 and Table 5, harmonic vibration durability of ENIG joints is seen to be significantly higher than that of OSP joints. Weibull plots and parameters for individual, unscaled stress groupings can be found in Appendix A.3.

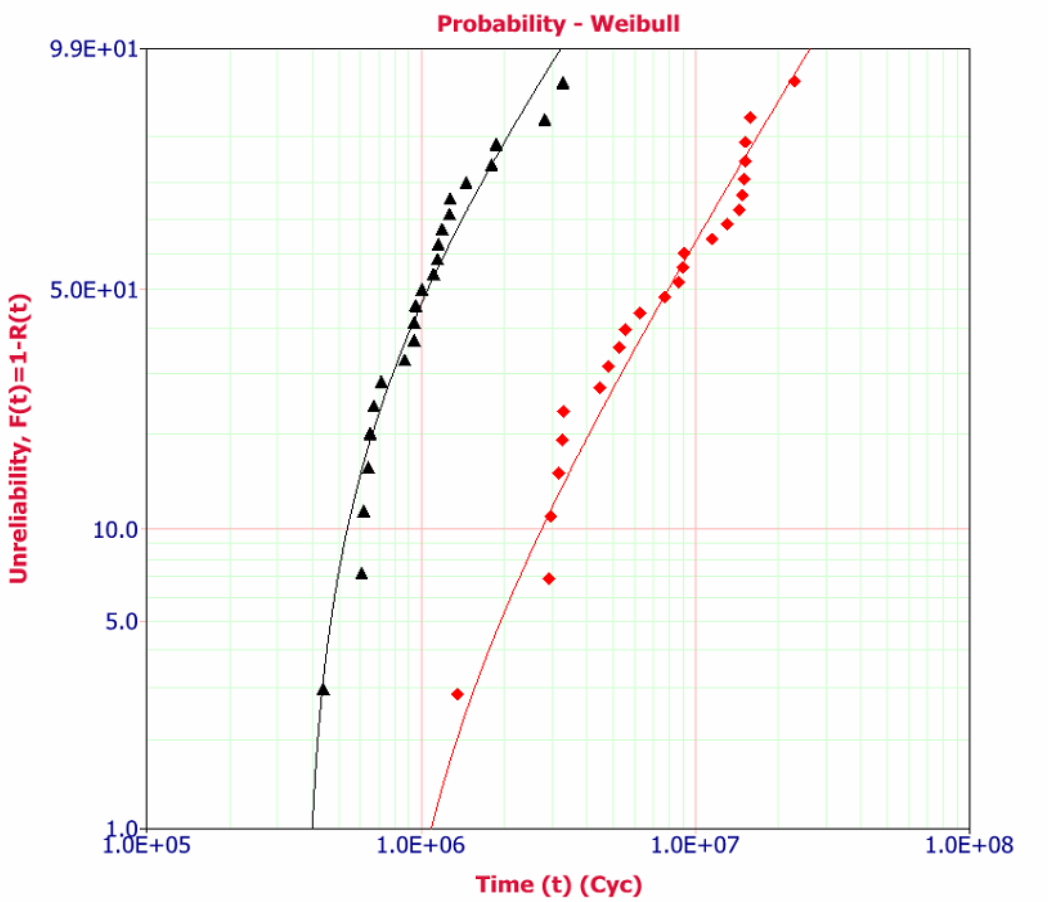

Figure 23: Three parameter Weibull fit to OSP vs. ENIG failure data from PWAs with no high-temperature aging

Weibull Parameters	OSP Aged 0 Hours	ENIG Aged 100 Hours
β	1.32	1.52
η	9.03E5	9.30E6
γ	3.72E5	6.43E5
Characteristic Life (η+γ)	**1.3E6**	**9.94E6**

Table 5: Weibull distribution fit parameters for OSP vs. ENIG failure data from PWAs with no high-temperature aging

4 Dynamic Finite Element Model

As explained in Chapter 1.5, harmonic vibration excitation is used because it is simpler to model and post process for the purposes of extracting solder S-N fatigue behavior under vibration loading. A dynamic finite element model (Figures 24, 25) I used to allow estimation of solder strains for a given PWB flexural strain. This provides a strain transfer function to map the PWB flexural response observed in-test to the corresponding strain history in the solder interconnect. Following common practice in the literature, a volume averaging scheme is employed for estimating the locally-averaged strain response in the vicinity of critical sites, to reduce FEA mesh sensitivity of the results. In this study, the volume-averaged strains are calculated from nodal strain values in two critical regions of the model, identified in Chapter 4.1.

4.1 Model Properties

The model assembly (Figure 24) is composed of two parts: the PWB and LCR. The PWB is modeled with 4-noded shell elements (FEA software element type – Kirchoff plate theory), and nodes are defined at the shell mid-plane. The LCR (which includes the ceramic body, copper pads and terminations, and SAC solder fillet) is modeled with 8-noded linear brick elements. Scaled structured meshing is used wherever possible, to achieve the appropriate mesh density as required. LCR dimensions are taken from data sheets provided by the manufacturer. The PWB and LCR parts are unified with a tie constraint between the top surface of the PWB and the bottom surface of the copper pads. The software uses multi-point constraint equations to tie the relevant nodes together. Since the FR4 board is 1.6mm thick, and

defined at the mid-plane, a tie constraint offset of 0.8mm is defined. Two versions of the FEA model are generated: one for the (100%) full pad LCRs and one for the (20%) narrow pad LCRs, pictured in Figure 25. A summary of mesh element counts can be found in Appendix A.1.

The model assumes a perfect clamped-clamped boundary condition at the two short edges of the board, pictured in red in Figure 24.

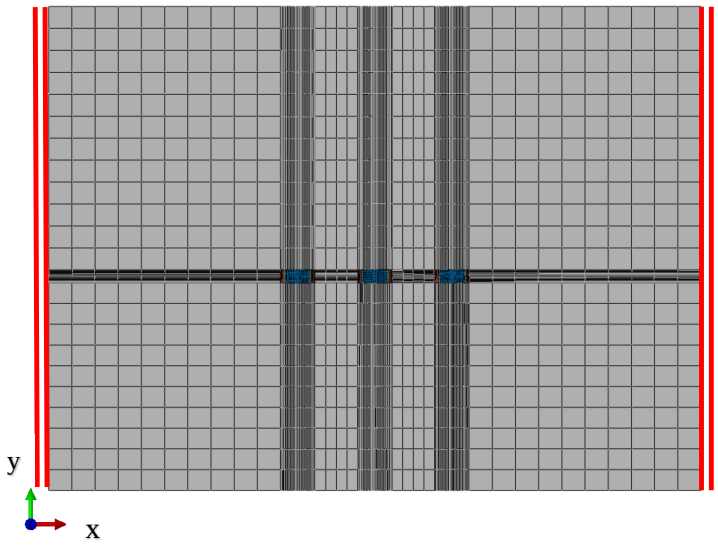

Figure 24: Board plane view of FEA assembly geometry, clamped along the short edges (red)

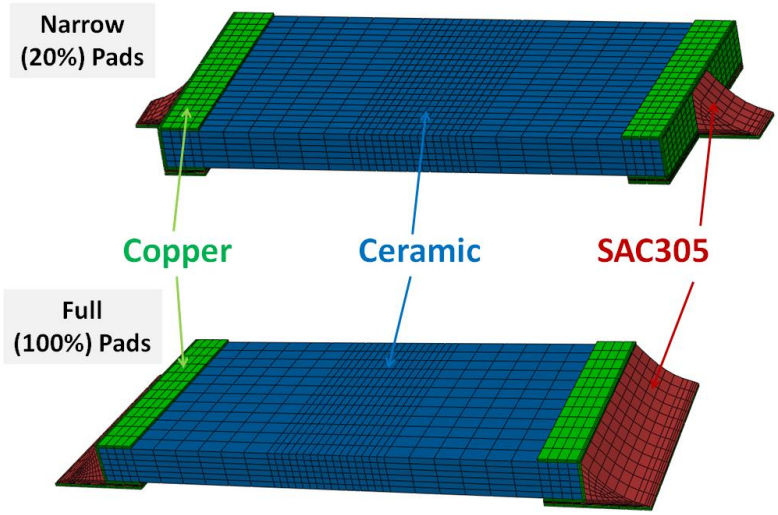

Figure 25: Narrow (20%) pad and Full (100%) pad LCR geometry

Due to lengthy simulation times, this finite element model simplifies the tested PWA such that only needed parts and materials are present. In particular only one representative LCR is modeled in each of the three columns 2, 3 and 4, since the mode shape of interest provides the same board curvature under all the components in each column. As discussed in Chapter 3.2, LCRs in Cols 1 and 5 are not investigated since their failures would not be achieved in a reasonable amount of testing time. As a result the LCRs in those columns are not modeled. The underlying simplifying approximation in these model simplifications is that the effect of the mass and stiffness of the remaining 37 LCRs (on the PWA modal behavior and dynamic response) is negligibly small and is therefore ignored.

The simulation settings allow for geometric nonlinearities (large deformations) in order to accurately account for plastic deformation of the SAC305 solder.

4.2 Material Properties

There are four important materials in the PWA that have to be considered in the model: (1) FR4 PWB, (2) ceramic LCR body, (3) copper pads, and (4) SAC305 solder. All constitutive material properties used within the model are presented in Appendix A.1.

The FR4 PWB is orthotropic and the elastic constants are approximated from values used in prior studies [45], by proportionate scaling of the elastic moduli to achieve the natural frequency of the PWA observed in-test. The ceramic and copper pads are modeled with linear isotropic elastic properties. The SAC305 solder is modeled as an elastic-plastic isotropic material, with constitutive relations obtained

from the literature. A base stress strain curve is taken from Darveaux and Banerji's work [46], chosen out of the numerous curves in the literature, because it was obtained via testing of joint size specimens, and at adequately high strain rates. Several other curves in the literature are obtained from bulk specimens, which do not accurately represent the grain sizes and microstructural effects of joint specimens. In addition, many are of strain rates too low to be representative of vibration. Darveaux's curve is at an estimated strain rate of 0.01/s.

Given the rate-sensitivity of solder stress-strain curves, it is clear that we need some estimate of the average strain rates of the tested specimens, in order to pick the right solder properties. Accounting for the high strain rate in harmonic vibration tests as an RMS value, and the volume of critical strain regions versus the entire solder fillet, strain rates of 0.05/s and 0.2/s are estimated for full pads and narrow pads, respectively. Using the Cowper-Symonds model [47], and rate-hardening constants from [48, 49], the base stress strain curve at 0.01/s is scaled to curves at 0.05/s and 0.2/s (Figure 26). This method of scaling constitutive properties for higher strain rates has been performed by other researchers to model loading such as drop/shock [50, 51]. Further discussion on how the Cowper-Symonds model is applied, and implications for future work are found in Appendix A.1.1.

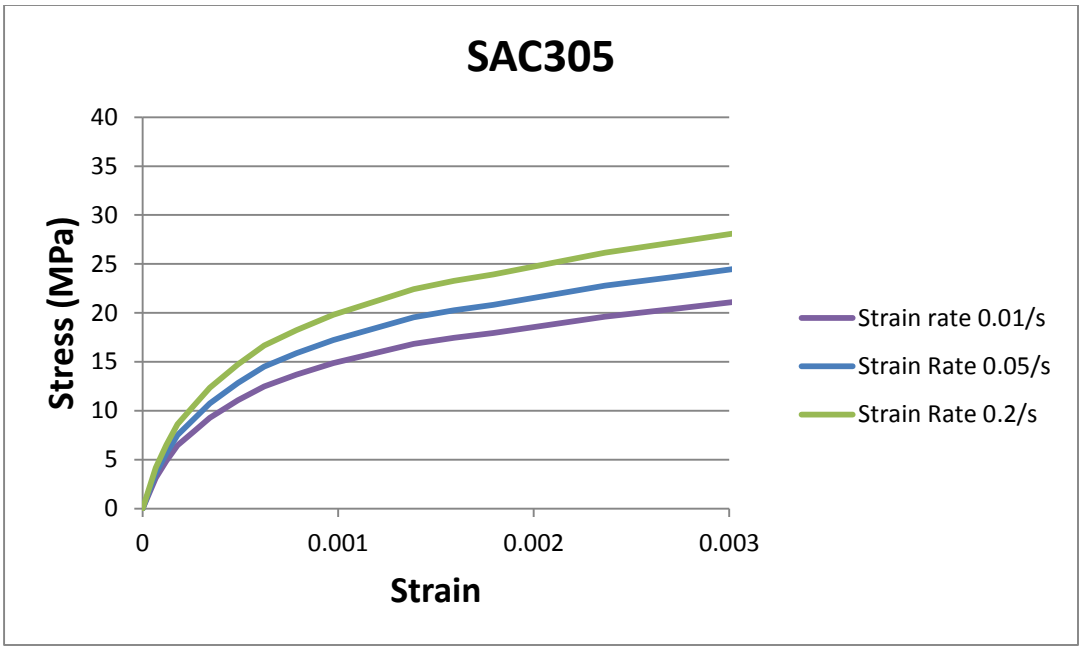

Figure 26: SAC305 stress strain curves scaled to desired strain rates

4.3 Time-Domain Dynamic Strain Analysis

Prior to the dynamic simulation, a modal analysis (Figure 27) is performed to ensure that the experimentally measured first natural frequency of the board is correctly represented by the FEA model. In addition, the mode shape is obtained so appropriate constraints can be used later for quasi-static modeling, as discussed later. In addition, the ratio of longitudinal board strains between Col 3 and Cols 2, 4 is obtained, so we can later infer the flexural strains at Cols 2, 4 from the strain-gage reading (which is located under Col 3).

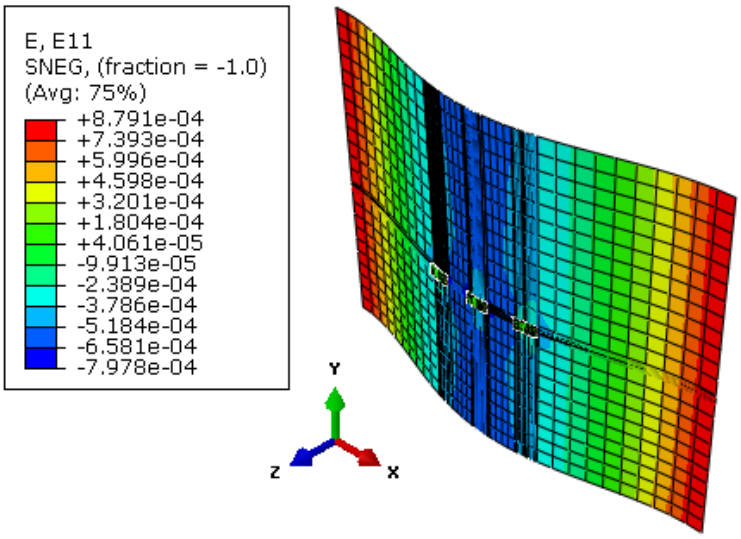

Figure 27: First mode shape with longitudinal strain visualization

For the dynamic simulation, a harmonic excitation is applied at the clamped edges (Figure 28) of the model, matching the in-test excitation frequency. The displacement response time history in the out-of-plane direction is monitored to ensure the dynamic simulation has achieved a steady-state response. The simulations are repeated for various harmonic displacement excitation levels at the clamped edges. In each case the corresponding von Mises board strain levels (at the location of the strain gage) and the corresponding volume averaged solder strain values are recorded.

Figure 28: Out of PWB-plane harmonic excitation direction (shell element thickness displayed)

4.4 Strain Transfer Functions

As discussed previously, the FEA results are used to construct a strain transfer function that maps PWB flexural response to respective SAC305 solder response. Two regions in the FEA model are selected to collect strain information for these transfer functions: (1) the strain gage footprint on the PWB, and (2) the region between the solder joint fillet and the PWB-side copper pad where the solder joint experiences the highest strain concentration. These regions are highlighted in Figure 29 for the full (100%) pad model. A detailed look at the mesh for the full pad resistor part can also be seen in the figure.

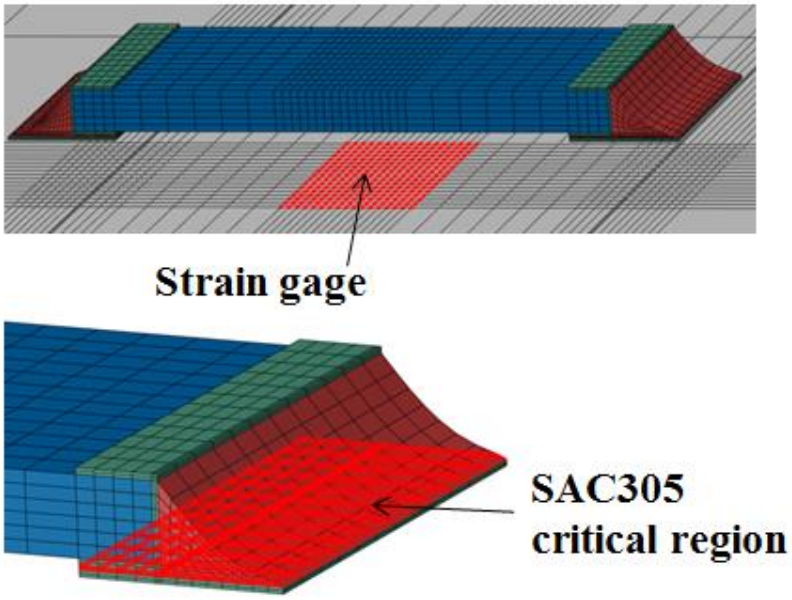

Figure 29: Critical region in FEA model for solder joint of LCR with full (100%) pad LCR and for strain gage region on PWB

Strains and volumes for elements within the SAC305 critical region are extracted in order to calculate the volumetric average value of equivalent strain within the solder critical region, at each excitation level. The formula for von Mises (equivalent) strain is presented in Equation 2. The bending strain at nodes in the strain

gage region of Figure 29 are also averaged to estimate the respective PWB strains for the transfer function.

$$\varepsilon_{eq} = \frac{\sqrt{2}}{3}\sqrt{(\varepsilon_{xx}-\varepsilon_{yy})^2 + (\varepsilon_{xx}-\varepsilon_{zz})^2 + (\varepsilon_{zz}-\varepsilon_{yy})^2 + 6(\varepsilon_{xy}^2+\varepsilon_{yz}^2+\varepsilon_{xz}^2)}$$

Equation 2: von Mises equivalent strain

Strain transfer functions are constructed for both the full (100%) pad and narrow (20%) pad cases, as seen in Figure 30.

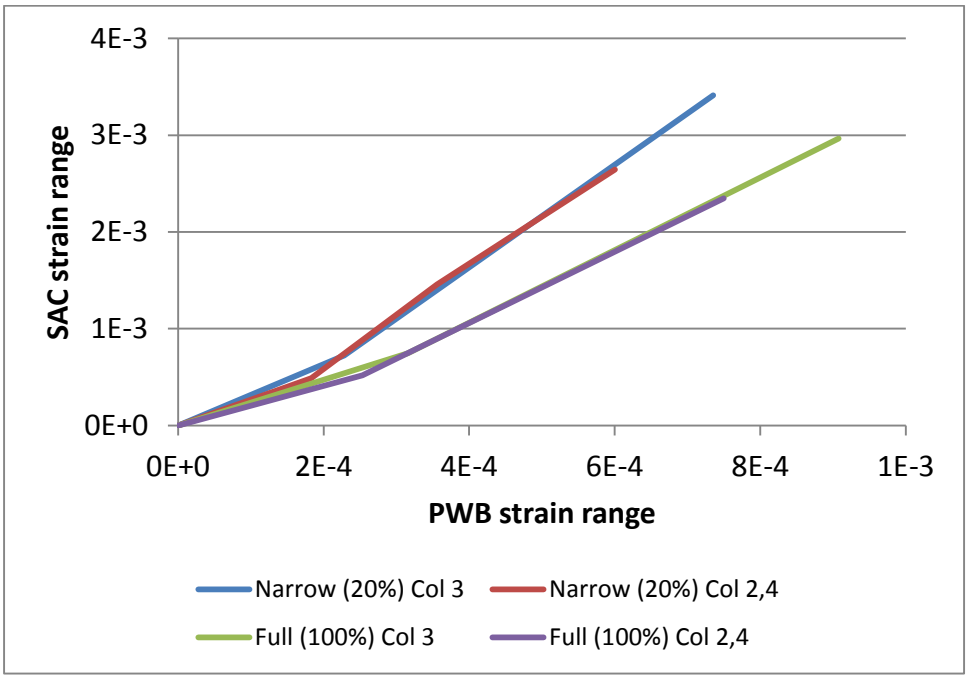

Figure 30: Strain transfer functions

As expected, the narrow pad experiences greater solder strains for the same PWB flexure due to the greater stress concentration in the smaller solder joint. To verify whether the strain transfer function depends on component location in the PWA, functions for both Col 3 and Cols 2, 4 are constructed and compared. As seen in Figure 30, the strain transfer functions are nearly identical (blue/red for narrow (20%) pads, and green/purple for the full (100%) pads).

4.5 Method for Reducing Simulation Time for Dynamic Problem: Initial Conditions

While a dynamic simulation is more representative than a quasi-static simulation for the vibration problem being modeled, a drawback is extensive computation time. If a time-domain simulation (simulation based on direct integration using time-stepping) is started at rest from an undeformed configuration, significant computational burden is placed on the CPU to overcome the initial transient solution and reach a steady state response. Ernst and Dasgupta [52] developed a method to minimize the initial transient portion of such a dynamic simulation, by applying suitable non-stationary initial conditions. Essentially the simulation commences on an undeformed model with initial velocities applied throughout the model to replicate a steady state response. This method is adapted in this study in order to produce strain transfer functions, which require increasingly large excitation levels.

Figure 31 demonstrates how varying distributions of initial velocities are applied. A beam is used an analogy to a PWB, for explanatory purposes. The illustration on top is of a beam with clamped ends and harmonic excitation applied. The grey lines represent the peak displacement configurations (positive and negative directions) that would be seen during a single cycle. This deformation geometry is based on the mode shape of the structure. The straight black line represents both the resting configuration and also the undeformed configuration during the transition between positive and negative deformations.

In order to determine the appropriate magnitudes for the initial velocities, the dynamic model is first simulated without initial velocities (meaning initial conditions

consist of zero velocities at all nodes) at a low excitation level, until a response at steady-state is achieved. The nodal velocities at the transition configuration during steady state response are extracted, then reapplied to the model as initial conditions. This imposes a steady state response at the onset of the simulation. The bottom illustration in Figure 31 shows the relative magnitudes of initial velocities which would be applied in this illustrative example.

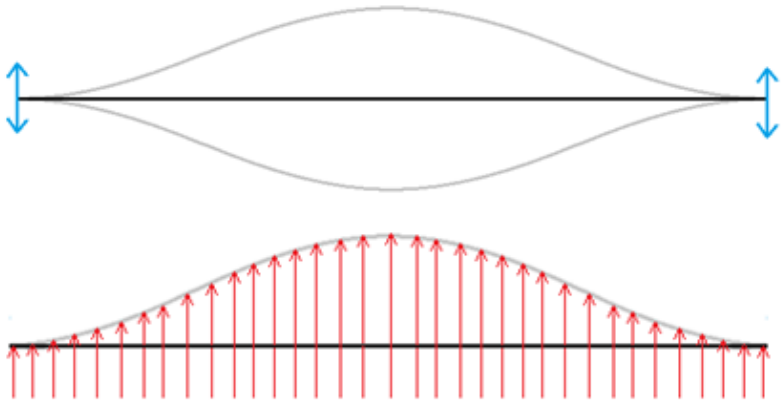

Figure 31: Beam mode shape displacement field (top), Initial velocity relative magnitudes (bottom)

For demonstration purposes, a model of a board with a single LCR in the center is used to compare differences in computation time (Figure 32). The same clamped boundary conditions and harmonic excitation discussed in Chapter 4.3 are applied.

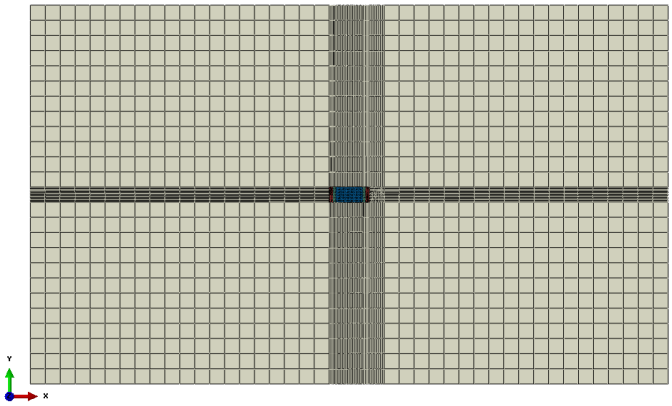

Figure 32: Simple LCR PWB model for computation time comparisons

By incrementing at reasonably small excitation levels, linear scaling of initial conditions can be used to generate a strain transfer function with reduced computation time. A sample transfer function for the model in Figure 32 is shown in Figure 33.

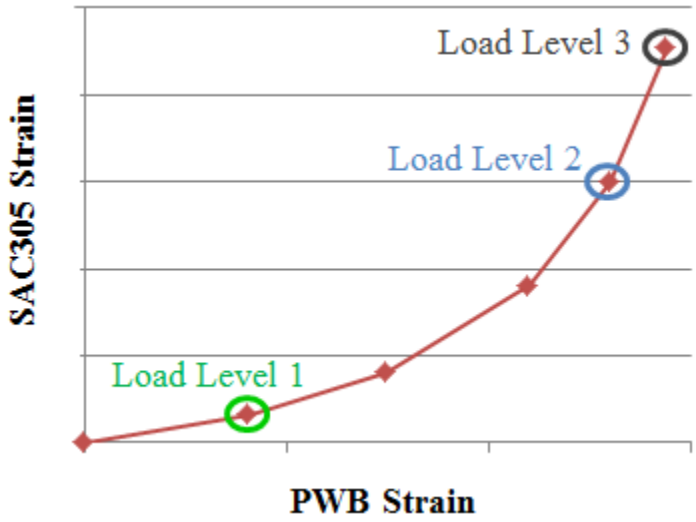

Figure 33: Sample strain transfer function

Caution must be taken as scaling to a large excitation level too quickly can further increase computation time. Figure 34 shows the displacement response at the center of the board for Load Level 3 in Figure 33 when the simulation is started from rest (initial conditions consist of zero velocities everywhere). There is a visible undershoot in the initial transient region before reaching a steady state response. Figure 35 demonstrates an initial overshoot due to poorly scaled initial conditions, when trying to scale directly from Load Level 1 to Load Level 3. Lastly Figure 36 shows the desired result of a displacement response which begins near steady state. In this case velocities were scaled from Load Level 2 to Load Level 3.

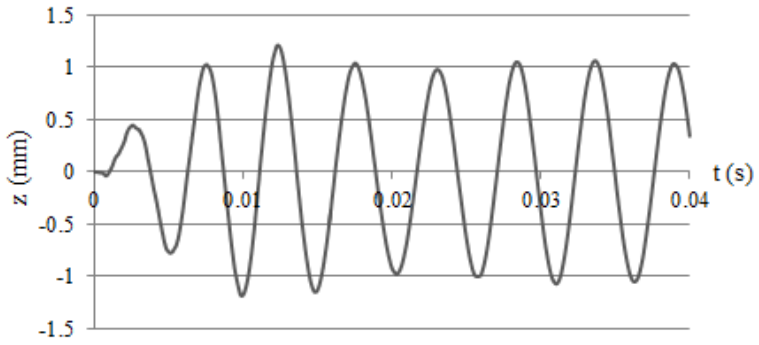

Figure 34: Displacement response without initial conditions

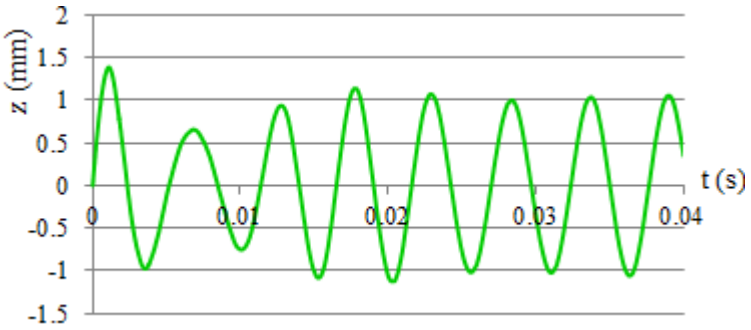

Figure 35: Displacement response with poorly-scaled initial conditions

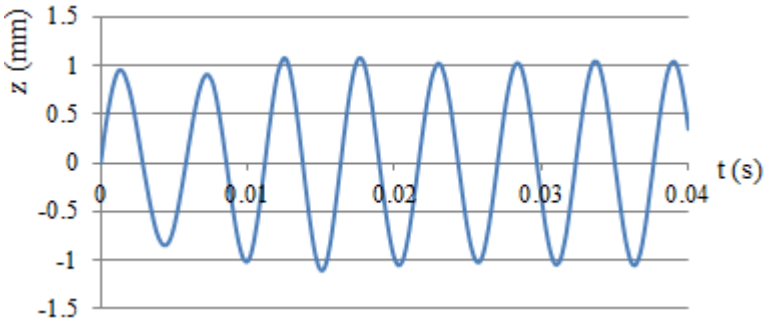

Figure 36: Displacement response with well-scaled initial conditions

In order to further decrease computation time, more powerful computing processors should be employed. Depending on how many CPU cores are utilized, simulation time can be decreased 6-9 times with well-scaled initial conditions. Table 6 demonstrates how no initial conditions, poorly scaled initial conditions, and well-scaled initial conditions can affect computation time, for both a typical 4-core CPU and a high performance computing cluster.

	No Initial Conditions	**Poorly-Scaled Initial Conditions**	**Well-Scaled Initial Conditions**
Desktop CPU 4 cores (3.20 GHz)	180 minutes	240 minutes	20 minutes
High Performance Computing Cluster 16 cores (2.80 GHz)	45 minutes		5 minutes

Table 6: Computation speed comparisons

5 Results: Effect of Aging on SAC305 Vibration Durability

In addition to the test results generated during this study, results are also available from prior harmonic vibration studies for SAC305 assemblies on OSP and ENIG boards of various architectures, with various different components, and various aging conditions. In order to allow comparison of results across all these heterogeneous sample sets, the effective solder S-N fatigue behavior is extracted from all the durability tests, using the time-domain finite element simulation described earlier in Section 4. To make comparisons with prior results self-consistent, the simulation conditions and solder constitutive relations were suitably tailored, to best replicate the modeling methods used for past results.

5.1 Summary of Data Sets

A summary is shown below for new data in Table 7, and for prior data from the literature in Table 8. SAC305 fatigue curve comparisons will be presented in Chapters 5.3-4.

New Data					
Data Set #	**Surface Finish**	**Component Type**	**Aging Condition**	**SAC305 Material Properties**	**Finite Element Simulation Conditions**
1a	OSP	LCR2512 (20% and 100% pads)	5 years @ Room Temp	Appendix A.1 Table 23, Figure 42	Dynamic
1b	OSP	LCR2512 (20% and 100% pads)	100 hours @ 125C + 5 years @ Room Temp	Appendix A.1 Table 23, Figure 42	Dynamic
1c	OSP	LCR2512 (20% and 100% pads)	500 hours @ 125C + 5 years @ Room Temp	Appendix A.1 Table 23, Figure 42	Dynamic
2	ENIG	LCR2512 (20% and 100% pads)	5 years @ Room Temp	Appendix A.1 Table X	Dynamic

Table 7: Summary of testing and modeling conditions for new data

Prior Data						
Data Set #	**Surface Finish**	**Component Type**	**Aging Condition**	**SAC305 Material Properties**	**Finite Element Simulation Conditions**	**Source**
3	OSP	HVQFN72	2 years @ Room Temp	Appendix A.1 Table 23, Figure 42	Quasi-static (Only Z direction of PWB nodes constrained)	[26]
4	OSP	LCR2512 and 1210 (100% pads)	100 hours @ 125C + unknown storage duration at room temperature	Appendix A.1 Table 23, Figure 42	Quasi-static (Only Z direction of PWB nodes constrained)	[25]
5	ENIG	LCR2512 (20% and 100% pads)	<1 year @ Room Temp	Appendix A.1 Table 23, Figure 42	Dynamic	[27]

Table 8: Summary of testing and modeling conditions for prior data

5.2 Fatigue Curve Bounds

As shown in failure analysis in Chapter 3.3.1, the failure data contain a mix of copper trace failures and solder joint failures. This is also true for prior test results. During the current study, the percent of solder failures are found to increase with cyclic strain amplitude. Some specimens are observed to have both trace cracks and solder cracks, with no means to determine which failure mode occurred first. Figure 37 below conceptually illustrates how this trend may be explained by deconstructing the data into a possible scenario of intersecting SAC305 solder S-N curves and copper trace S-N curves.

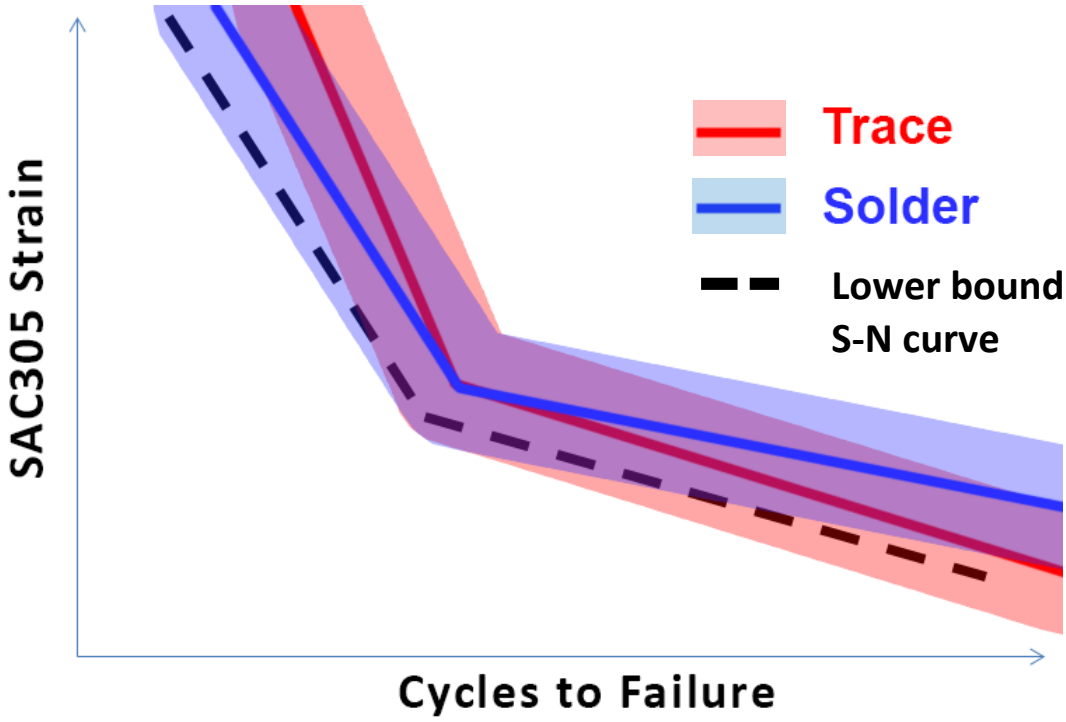

Figure 37: Conceptual schematic for possible S-N curves for trace and solder with confidence bounds

The solid red line conceptually represents the copper trace S-N curve, and the surrounding low-opacity red distribution represents confidence bounds to account for

statistical scatter. Similarly the solid blue line represents the SAC305 solder S-N curve, with a low-opacity blue confidence bound distribution. For convenience of depiction (but without loss of generality), the two curves are shown in this example illustration to cross over at the transition region between low cycle and high cycle fatigue. The black dashed line serves as the leftmost envelope, or lower bound, of the collection of the two curves, representing the fatigue curve produced from this study. Observing the overlaps with the dashed lower bound curve: the HCF (high-cycle fatigue) region of the plot (below the transition region) will be dominated by the distribution of trace failures, while the LCF (low-cycle fatigue) region will be dominated by the distribution of solder failures. Thus the material fatigue curves presented in Chapter 5.3 serve as lower bounds for SAC305 fatigue curves. The true SAC305 S-N curves could lie somewhere to the right of these lower bound curves.

5.3 SAC-OSP Fatigue Curves as a Function of High Temperature Aging

Combining the accelerated test results from Chapter 3 with the SAC305 strains found in Chapter 4, material fatigue curves for SAC305 are produced for data sets 1a-c of Table 7. The Weibull characteristic lives of failure times in each stress level grouping from Table 3 are used to construct these S-N curves. Complete Weibull statistical fits for all stress levels can be found in Appendix A.3. The SAC305 strains for both pad types at each response level are found using their respective transfer functions (Figure 30), corresponding to the board strain measured in-test. The resulting SAC305 material fatigue curves shown in Figure 38 indicate that high temperature isothermal aging decreases SAC305 harmonic vibration durability, with the severity of the effect increasing as the stress levels increase.

Using the power law fits inlaid onto Figure 38, the normalized change in vibration durability with respect to high temperature aging, at the highest and lowest stress levels on the PWA, is summarized in Table 9.

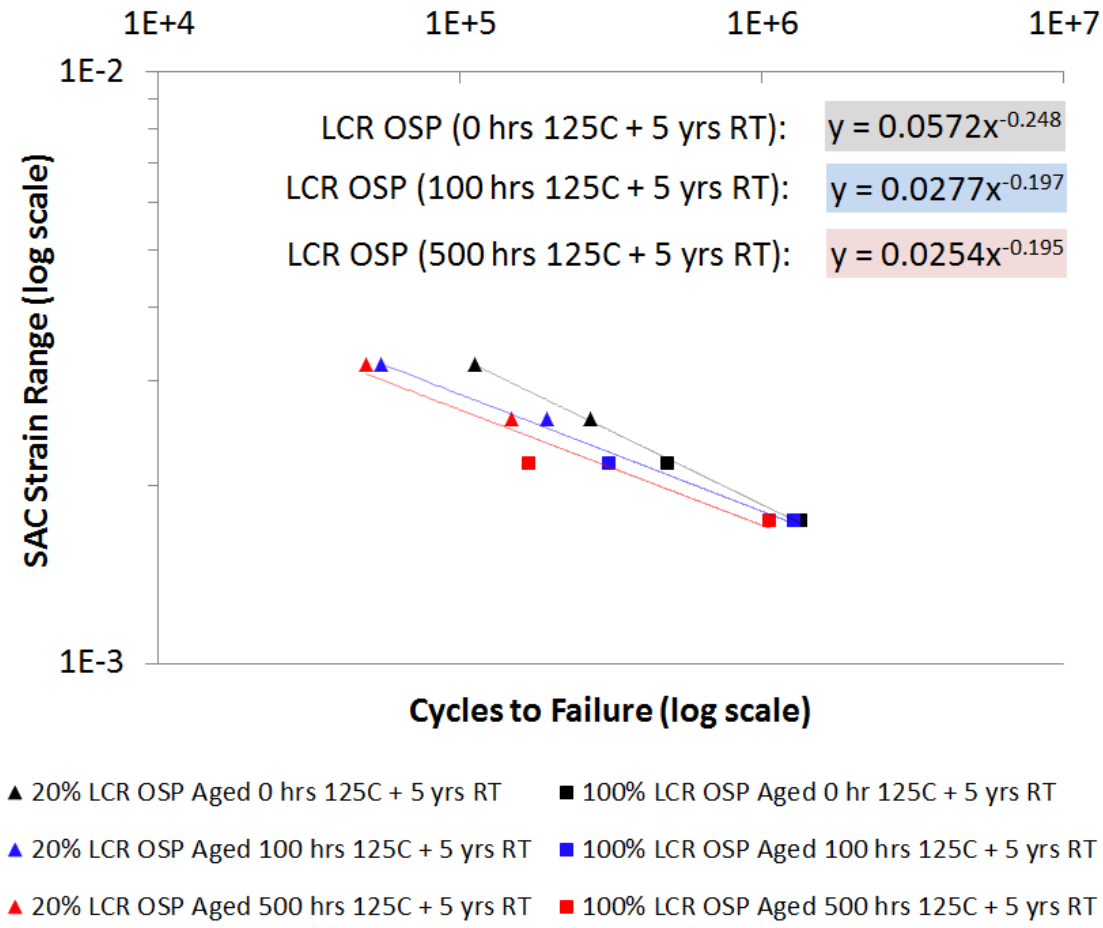

Figure 38: SAC305/OSP fatigue curves as a function of high temperature aging (Data sets 1a-c per Table 7)

LCR2512/OSP PWAs	Normalized Change in Life		
	Aged 0 hrs 125°C + 5 yrs RT	Aged 100 hrs 125°C + 5 yrs RT	Aged 500 hrs 125°C + 5 yrs RT
Highest Stress Level at Narrow (20%) Col 3	1	0.51	0.37
Lowest Stress Level at Full (100%) Col 2,4	1	0.97	0.72

Table 9: Change in SAC305/OSP LCR2512 vibration durability with respect to high temperature aging (Data sets 1a-c per Table 7)

Using only the Basquin (HCF) portion of the Basquin-Coffin-Manson fatigue model, the power law fit in Figure 38 can be used to extract fatigue model constants (σ_f/E, b). The form of the power law fits inlaid onto Figure 38 is in Equation 3, and the Basquin fatigue constants are summarized in Table 10. This same method is applied to the fatigue curves in Figures 39-41.

$$\Delta\boldsymbol{\varepsilon} = \mathbf{2} * \frac{\boldsymbol{\sigma_f}}{\boldsymbol{E}} (\mathbf{2}\boldsymbol{N_f})^{\boldsymbol{b}}$$

Equation 3: Basquin (HCF) Fatigue Model

LCR2512/OSP PWAs	σ_f/E	b
Aged 0 hrs 125°C + 5 yrs RT	0.0286	-0.248
Aged 100 hrs 125°C + 5 yrs RT	0.01385	-0.197
Aged 500 hrs 125°C + 5 yrs RT	0.0127	-0.195

Table 10: Basquin fatigue model constants (Data sets 1a-c per Table 7)

5.4 Comparison of Data Sets

Although all of the data sets from Tables 7 and 8 are results of harmonic vibration durability tests for SAC305 assemblies, they cannot be directly compared since their testing parameters and assembly configurations differ. However, results can be compared when they are transformed to the same damage metric—solder strain, via use of the strain transfer functions. Due to differences in material properties and finite element simulation techniques used in prior studies, individualized strain transfer functions are developed for comparison to each case. The resulting fatigue curves are compared within this section.

5.4.1 SAC305-ENIG, OSP Boards (LCR2512) Aged Various Durations at Room Temperature

Data sets 1a, 2, and 5 of Tables 7 and 8 all contain SAC305 LCR2512 assemblies without any additional aging beyond extended room temperature storage. Data set 5 is from harmonic vibration testing of SAC305/ENIG boards of the same configuration, in the same fixturing and test setup as the current study—although conducted 5 years earlier [27]. Thus, SAC strains for all data sets were obtained using the same transfer functions shown in Figure 30. The fatigue curves in Figure 41 feature two comparisons: (i) OSP versus ENIG boards for the same aging condition (5 years room temperature storage), and (ii) ENIG boards of different aging conditions (<1 year versus 5 years room temperature storage). At low stress levels ENIG joints clearly outperformed OSP joints, but at high stress levels there was much less difference. There is a clear decrease in harmonic vibration durability among ENIG boards as the storage duration increases from <1 year to 5 years at room temperature.

Using the power law fits inlaid onto Figure 39, the normalized change in vibration durability with respect to surface finish, at the highest and lowest stress levels (in the ENIG board aged 5 years at room temperature), is summarized in Table 11. Similarly, the normalized change with respect to room temperature aging, in the highest and lowest stress levels (in the ENIG PWA aged <1 year at room temperature) is summarized in Table 12. Basquin fatigue model constants are summarized in Table 13.

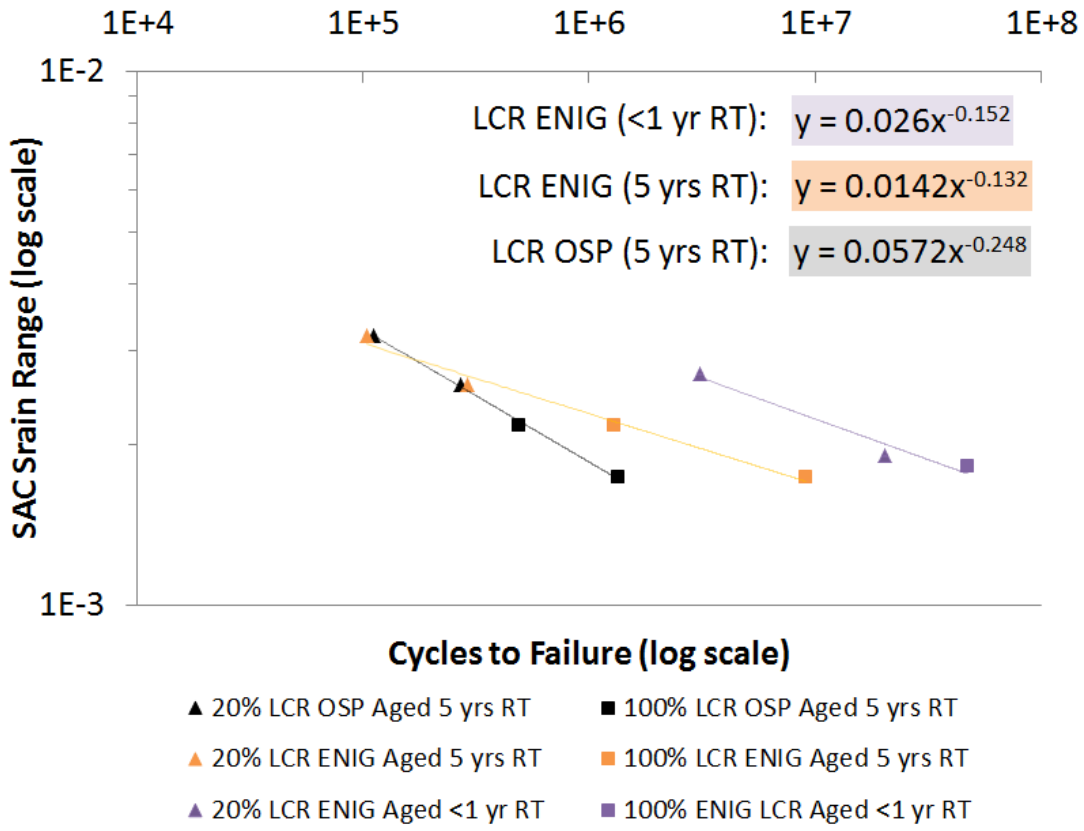

Figure 39: SAC305/OSP, SAC305/ENIG fatigue curves for no additional aging beyond storage (Data sets 1a, 2, 5 per Tables 7, 8)

LCR2512/ENIG PWA vs. LCR2512/OSP PWA	Normalized Change in Life	
	ENIG Aged 5 yrs RT	OSP Aged 5 yrs RT
Highest Stress Level at Narrow (20%) Col 3 (on ENIG PWAs Aged 5 yrs RT)	1	1.4
Lowest Stress Level at Full (100%) Col 2,4 (on ENIG PWAs Aged 5 yrs RT)	1	0.16

Table 11: Change in SAC305 vibration durability with respect to surface finish (Data sets 1a, 2, per Table 7)

LCR2512/ENIG PWAs	Normalized Change in Life	
	ENIG Aged <1 yr RT	ENIG Aged 5 yrs RT
Highest Stress Level at Narrow (20%) Col 3 (on ENIG PWA Aged <1 yr RT)	1	0.10
Lowest Stress Level at Full (100%) Col 3 (on ENIG PWA Aged <1 yr RT)	1	0.14

Table 12: Change in SAC305/ENIG vibration durability with respect to room temperature aging (Data sets 2, 5 per Tables 7, 8)

LCR2512/ENIG PWAs	σ_f/E	b
ENIG Aged <1 yr RT	0.013	-0.152
ENIG Aged 5 yrs RT	0.0071	-0.132

Table 13: Basquin fatigue model constants (Data sets 2, 5 per Tables 7, 8)

5.4.2 SAC305-OSP Boards (LCR2512, HVQFN72) Aged 2-5 Years at Room Temperature

Board assemblies with arrays of HVQFN72s were tested under harmonic excitation, with an OSP surface finish [26]. In Choi's study, a 3D finite element model was developed to estimate the strain history in the critical solder joints, pictured in Figure 40 [53]. The PWB was modeled with shell elements and the component was modeled with 3D brick elements that were tied to the PWB surface. This is the same modeling strategy used in the current study. Choi modeled the QFN component at the PWB center in sufficient detail to assess the solder strain. The remaining QFN components were approximately represented by accounting for their stiffening effect and for their added mass, on the properties (stiffness and density) of the PWB elements that fall within the foot-print of each QFN component. To produce the strain transfer function between the PWB flexural strain and the averaged

strain in the critical region of the solder, Choi exercised this finite element model in a quasi-static manner, in which only out-of-board plane displacements of the PWB were constrained to follow the fundamental mode shape of the PWA. This constraint was applied using multi-point constraint equations, based on the central node of the PWB as the master node, for reference purposes. The in-plane translational DoFs and the rotational DoFs of the nodes in the PWB shell elements were not constrained in any way.

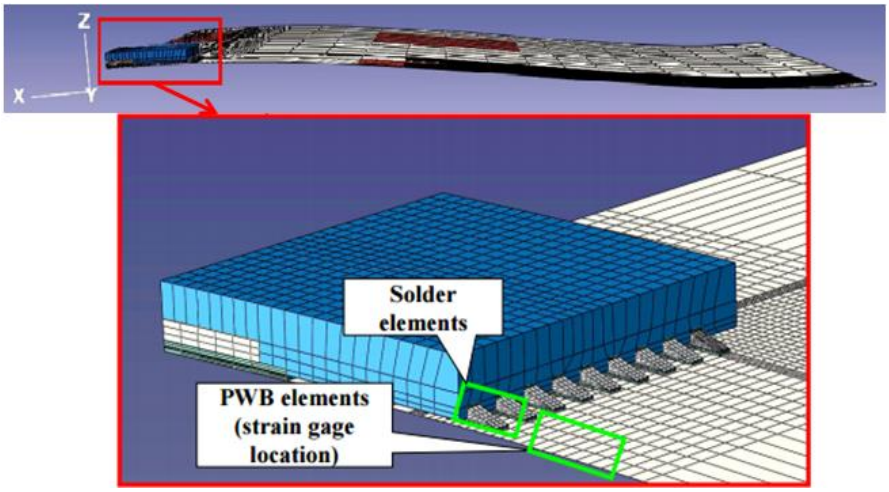

Figure 40: HVQFN72 3D quasi-static quarter model [53]

To enable meaningful comparison, this modeling technique was replicated with the LCR2512 model of this study, using the same SAC305 material properties as those in the HVQFN72 model (Appendix A.1 Table 10, Figure 44, Data set 3). Choi's specimens were not aged additionally beyond 2 years of room temperature storage, so the data is compared to results from the current study for SAC305/OSP LCR2512 assemblies with no additional aging beyond 5 years of storage. The fatigue curves in Figure 41 show that the additional years of room temperature aging apparently decreased the harmonic vibration durability slightly for lower stresses, and

with less effect at higher stresses. The differences in component architecture, and thus simplifications and assumptions in finite element modeling, may be obfuscating results.

Using the power law fits inlaid onto Figure 41, the normalized change in vibration durability with respect to room temperature aging, in the highest and lowest stress levels (in the HVQFN/OSP PWA aged 2 years at room temperature), is summarized in Table 14. Basquin fatigue model constants are summarized in Table 15.

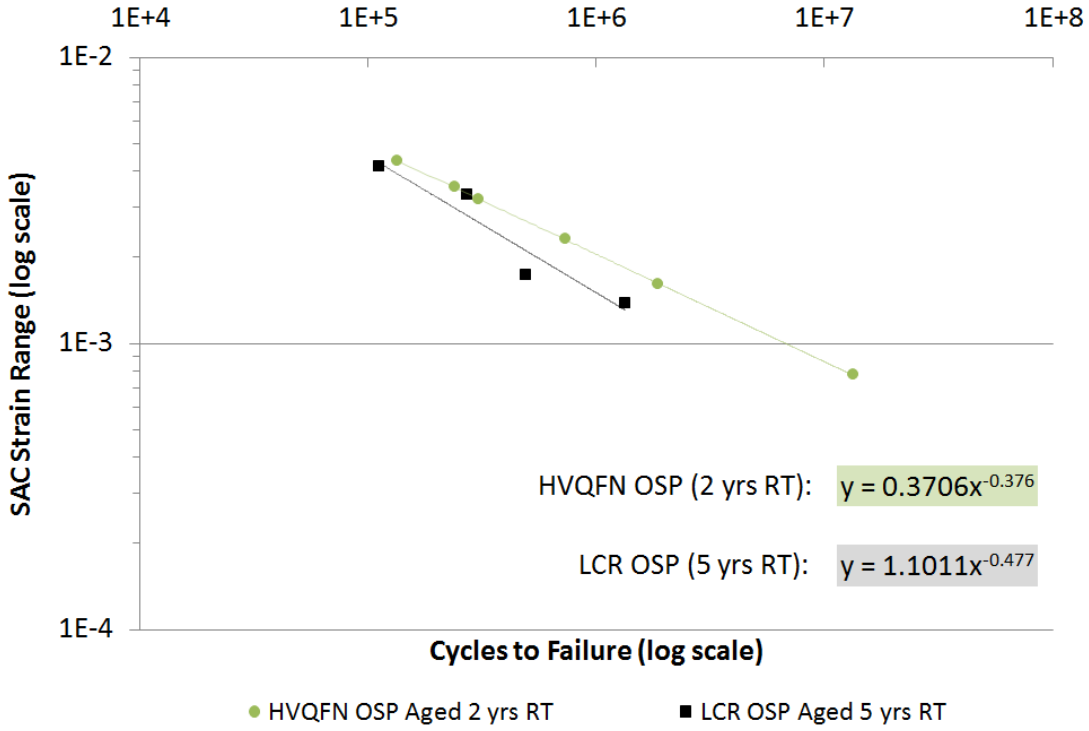

Figure 41: SAC305/OSP fatigue curves for no additional aging beyond room-temperature (Data sets 1a, 3 per Tables 7, 8)

LCR2512/OSP PWA vs. HVQFN/OSP PWA	Normalized Change in Life	
	HVQFN/OSP Aged 2 yrs RT	LCR2512/OSP Aged 5 yrs RT
Highest Stress Level (on HVQFN PWA Aged 2 yrs RT)	1	0.80
Lowest Stress Level (on HVQFN PWA Aged 2 yrs RT)	1	0.30

Table 14: Change in SAC305/OSP vibration durability with respect to room temperature aging (Data sets 1a, 3 per Tables 7, 8)

LCR2512/OSP PWA vs. HVQFN/OSP PWA	σ_f/E	b
HVQFN/OSP Aged 2 yrs RT	0.1853	-0.376
LCR2512/OSP Aged 5 yrs RT	0.55055	-0.477

Table 15: Basquin fatigue model constants (Data sets 1a, 3 per Tables 7, 8)

5.4.3 SAC305-OSP boards (LCR2512/1210) with 100 Hours of Aging @ 125°C After Various Durations of Room Temperature Storage

PWAs in data set 4 of Table 8 included the same 2512 LCRs as those in this study, as well as some 1210 resistors. Specimens in data set 4 were aged 100 hours @ 125°C after an unknown duration of room temperature storage, so their results are compared to those of specimens aged in the present study for 100 hours @ 125°C after 5 years of room temperature storage. The original finite element model used to produce the strain transfer function in [25] was a quasi-static 2D plane-stress finite element model, where the PWB, LCR components and solder interconnects were all modeled with 2D 4-noded plane-stress elements (Figure 42).

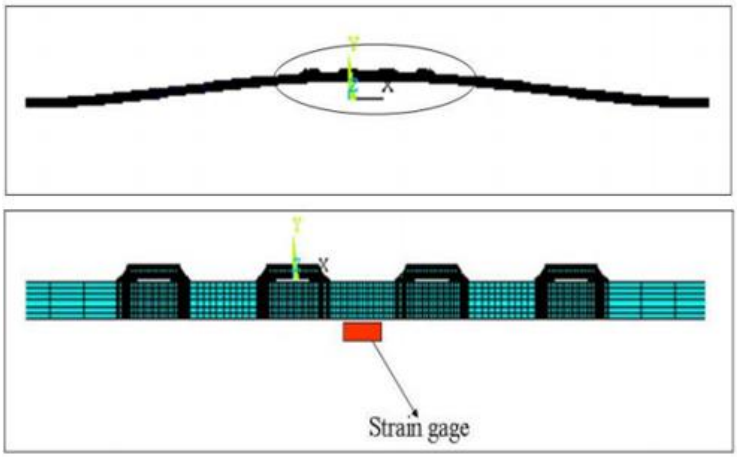

Figure 42: LCR2512 2D quasi-static model [25]

In contrast, a 3D quasi-static model (with 4-noded shell elements for the PWB, and 8-noded brick elements for components and interconnects) is used in the present study to construct the strain transfer function, using the same material properties as the model in in Figure 42 (Data set 4, Table 15 and Figure 44). As in Choi's study [26], Zhou constraints only out-of-board plane displacements at the PWB (bottom surface) with multi-point constraint equations, to mimic the mode shape of the PWB in her quasi-static simulation. The in-plane translation DoFs are left unconstrained. To match the deformation field of Zhou's model as closely as possible, the present study uses the same out-of-plane modal displacement constraints that were described earlier in Chapter 5.4.2. However, it is understood that there are still differences in the displacement fields of Zhou's study and the current study, due to the differences in the 2D vs 3D modeling strategies.

The resulting fatigue curves in Figure 43 apparently show a very significant decrease in harmonic vibration durability compared to that of LCR2512/1210s in [25]. The difference can be attributed in part to the additional 5 years of storage at room temperature, prior to aging 100 hours at 125°C. In addition to the difference in room temperature aging, discrepancies in finite element modeling techniques (2D vs. 3D models), and definitions in failure criteria, may be exacerbating the disparity between the fatigue curves. Since the LCR2512/1210 board achieved failure times orders of magnitude greater than those in this study, for even larger board strains, there may also be a fundamental difference between the boards tested.

Using the power law fits inlaid onto Figure 43, the normalized change in vibration durability with respect to room temperature aging is summarized in Table

16, for the highest and lowest stress levels (on the LCR/OSP PWA Aged 100 hours @ 125°C). Basquin fatigue model constants are summarized in Table 17.

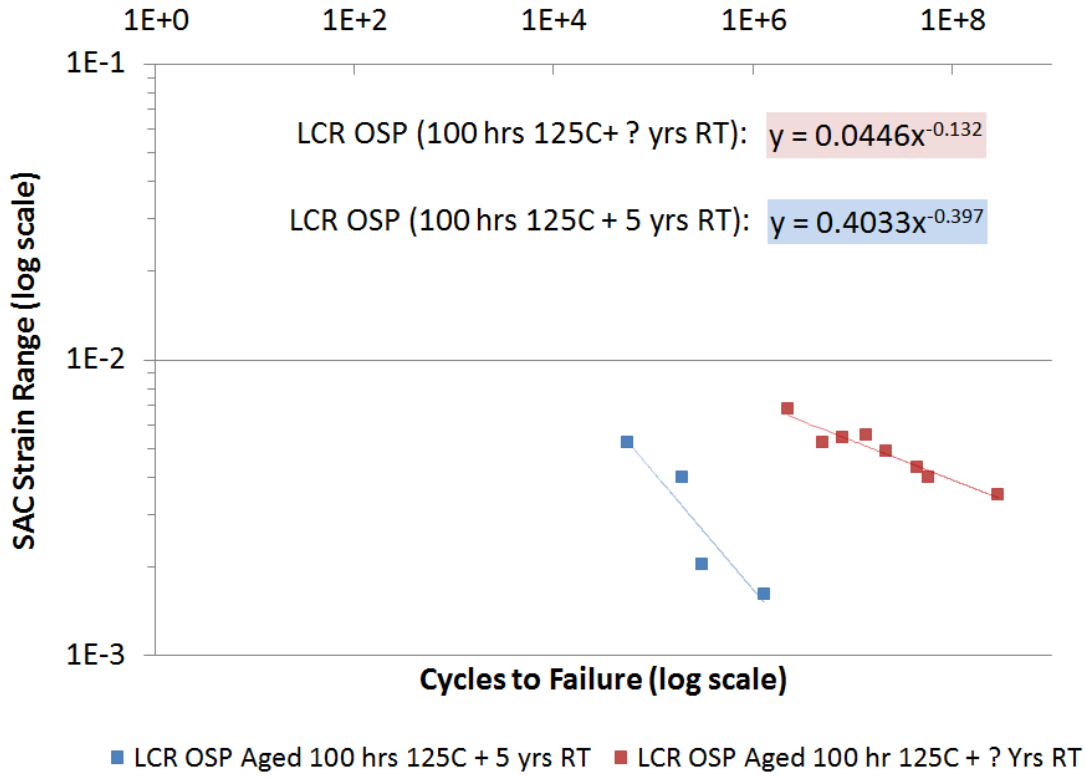

Figure 43: SAC305/OSP fatigue curves (Data sets 1b, 4 per Tables 7, 8)

LCR2512,1210/OSP PWA vs. LCR2512/OSP PWA	Normalized Change in Life	
	LCR2512,1210/OSP Aged 100 hrs 125°C + ? yrs RT	LCR2512/OSP Aged 100 hrs 125°C + 5 yrs RT
Highest Stress Level (on LCR2512/1210 PWA Aged 100 hrs 125°C + ? yrs RT)	1	0.020
Lowest Stress Level (on LCR2512/1210 PWA Aged 100 hrs 125°C + ? yrs RT)	1	6.5E-4

Table 16: Change in SAC305/OSP vibration durability with respect to room temperature aging (Data sets 1b, 4 per Tables 7, 8)

LCR2512,1210/OSP PWA vs. LCR2512/OSP PWA	σ_f/E	b
LCR2512,1210/OSP Aged 100 hrs 125°C	0.0223	-0.132
LCR2512/OSP Aged 100 hrs 125°C + 5 yrs RT	0.20165	-0.397

Table 17: Basquin fatigue model constants (Data sets 1b, 4 per Tables 7, 8)

6 Conclusions, Contributions, Future Work

The culmination of experimental testing and finite element simulation and yielded S-N fatigue curves for SAC305 as a function of aging, for OSP/Cu and ENIG/Cu metallizations. The major conclusions, contributions, and future tasks for this study are summarized in this Chapter.

6.1 Conclusions

The resulting SAC305 material fatigue curves shown in Figure 38 indicate that isothermal pre-aging decreases SAC305 harmonic vibration fatigue. At lower stress levels a longer time is needed to see the effects of aging, whereas at higher stress levels the effects can be seen much sooner (Table 9). Failure analysis of specimens corroborates observations in the literature about the effects of extended aging on SAC elastic-plastic behavior, and microstructure (bulk and interfacial IMC morphology and composition). Extended high temperature aging yielded thick, flattened, multi-layered and brittle interfacial IMCs, as well as coarser bulk IMCs. These effects are seen to contribute to more rapid solder cracking failure modes in vibration fatigue.

SAC/OSP and SAC/ENIG PWAs of identical room temperature aging conditions displayed significantly greater durability in ENIG PWAs for low stresses but less of a difference for high stresses (Table 11). Qi et. al. observed greater vibration durability of SAC/ENIG PWAs over SAC/OSP PWAs of identical aging conditions, although for step-stress random vibration loads [23]. The variation in vibration durability across surface finishes is likely due to the influence of surface finish on interfacial IMCs (discussed in Chapter 2).

Comparisons of SAC assemblies with various amounts of room temperature storage suggest that isothermal room temperature aging also generates appreciable reductions in vibration durability (Table 12 presents a comparison which is the least approximate, for ENIG boards of different storage durations).

In terms of stress analysis, harmonic vibration is determined to be more viable than random vibration for extracting solder material fatigue curves. Lower excitation levels are required in-test to generate failures in reasonable time, and post-processing of harmonic excitation is simpler due to the constant amplitude and uni-modal response. Lastly, time-domain dynamic FEA offers a convenient way to account for nonlinearities in solder behavior. While this is computationally intensive to achieve steady state response, proper setup of the initial conditions can significantly reduce simulation time. Finally, the cyclic fatigue curves extracted from vibration tests depend entirely on the stress-strain behavior assumed for the material, so fatigue models and stress-strain models should always be presented as paired properties.

6.2 Contributions

This study has provided:

- Isothermal aging-dependent SAC305 fatigue curves in the literature, for OSP/Cu and ENIG/Cu metallization.
- Insights into the effects of high temperature aging on vibration durability, as well as extended room temperature aging.
- Insights into creating a dynamic time-domain model for harmonic vibration durability, made computationally economical with proper initial conditions.

- Insights into how to estimate material properties which are appropriate for the estimated strain rates, for vibration simulation.

6.3 Future Work

Further improvements can be made to the experimental study, as well as the finite element simulation techniques.

6.3.1 Future Work for Experimental Study

Failure analysis of additional components would provide greater insight into the effects of aging on harmonic vibration fatigue. Due to time and resource limitations cross sections could not be produced for all failed components in this study (3 boards, with 24 components per board = 72 LCRs in total). However, it would be informative to obtain more definite data on the percentages of solder and trace crack failure modes. Additionally further investigations need to be made for SAC assemblies without extensive storage aging conditions. A comparison with as-reflowed solder should be made to further characterize the effect of aging on microstructure.

Several steps can be taken to improve the experimental setup towards extracting SAC305 S-N curves. The resistor board design or fixture design may be modified to allow for even more stress levels for increased detail in the S-N curve. In the case of this investigation, the resistors in Cols 1, 5 were unable to be used for failure data due to their placement at regions of low board curvature for the first mode shape. Components may be rearranged, or both sides of the board may be utilized, to increase the number of stress levels. Increasing the number of LCRs would also increase the number of replicates at a given stress level, thus improving the statistical

significance of the results. Also, alternative PWA manufacturing specifications should be employed in order to reduce the number of trace crack failures. The copper traces should be thicker, and employ a teardrop pad design to increase their fatigue life above that of the solder.

In addition, to explore the influence of the specimen architecture on the SAC305 S-N curves, the study should be expanded to include for larger, complex active components such as BGAs, QFPs, and PLCCs, and also different thickness and stiffness of multilayer PWBs. To expand the investigation of harmonic vibration durability of solders, the methodology can be repeated for other solder and surface finish combinations.

6.3.2 Future Work for Finite Element Simulation

Continued refinement of the FEA model is needed in terms of material properties. The model used unaged SAC305 stress strain curves for the dynamic simulation. However those curves are not fully representative of the testing and material parameters of this study. Isothermal aging affects the stress-strain behavior of SAC305 and in turn alters the obtained strain transfer functions. Further work is needed to improve the accuracy of the in-test material behavior and the extracted fatigue curves. Joint-scale testing of SAC305 specimens aged 0, 100, 500 hours at 125C should be conducted to obtain aging-dependent stress-strain curves. However, this still would not account for the 5 years of room temperature storage in PWAs for this study. Additionally, material stress-strain curves change due to progressive vibration fatigue. Dynamic microstructural recrystallization is observed in solder joints under isothermal, mechanical cycling [54, 55], in the form of reduced grain

sizes, especially near cracks. Material constants should be updated as a function of cumulative fatigue degradation to account for the effects of dynamic recrystallization.

In addition to applying age-sensitive material properties, rate-sensitive properties are needed as well. In Chapter 4.2 (further explained in Appendix A.1.1), an iterative scheme is proposed to determine the appropriate average strain rate required for estimating the appropriate SAC305 stress strain curve. However that is only an approximation, as the solder joint has a non-uniform strain (and strain-rate) distribution, and hence different parts of the solder joint will follow different stress-strain curves. A more robust development is to integrate a rate-sensitive material constitutive model e.g. the Cowper-Symonds model [47] or the Johnson-Cook model [56] into the finite element model.

In terms of boundary conditions, future models should include some torsional compliance in the clamped short edges. In reality clamping conditions are not perfect and this affects the board response in-test.

Appendices

A.1 FEA Model Properties

Table 18 states the size of each major element set in the FEA models.

Model Version	Set	# of Elements
Full (100%) Pad Model	PWB	7448
	PWB critical region	256
	SAC (one side)	1080
	SAC critical region	504
Narrow (20%) Pad Model	PWB	7052
	PWB critical region	256
	SAC (one side)	1000
	SAC critical region	420

Table 18: Mesh element count for FEA models

A.1.1 FEA Model Material Properties

FR4 PWB orthotropic elastic material properties are adapted from [45], with proportionate scaling of elastic moduli to achieve the natural frequency of the PWA observed in-test. D1111-D2323 in Table 19 are constants in the elastic stiffness matrix, defined by the FEA software package in Equation 4. Table 20 provides the same orthotropic elastic material properties, but in terms of elastic moduli, shear moduli, and Poisson's ratios.

Density (10^3 kg/mm^3)	D1111	D1122	D2222	D1133	D2233	D3333
2E-9	13278.7	1814.6	13278.7	1765.9	1765.9	6641.6

D1212	D1313	D2323
3700	2900	2900

Table 19: FR4 PWB Orthotropic Elastic Material Properties (as entered into finite element software)

$$\begin{Bmatrix} \sigma_{11} \\ \sigma_{22} \\ \sigma_{33} \\ \sigma_{12} \\ \sigma_{13} \\ \sigma_{23} \end{Bmatrix} = \begin{bmatrix} D_{1111} & D_{1122} & D_{1133} & 0 & 0 & 0 \\ & D_{2222} & D_{2233} & 0 & 0 & 0 \\ & & D_{3333} & 0 & 0 & 0 \\ & & & D_{1212} & 0 & 0 \\ & sym & & & D_{1313} & 0 \\ & & & & & D_{2323} \end{bmatrix} \begin{Bmatrix} \varepsilon_{11} \\ \varepsilon_{22} \\ \varepsilon_{33} \\ \gamma_{12} \\ \gamma_{13} \\ \gamma_{23} \end{Bmatrix} = [D^{el}] \begin{Bmatrix} \varepsilon_{11} \\ \varepsilon_{22} \\ \varepsilon_{33} \\ \gamma_{12} \\ \gamma_{13} \\ \gamma_{23} \end{Bmatrix}.$$

$$\begin{aligned}
D_{1111} &= E_1(1-\nu_{23}\nu_{32})\Upsilon, \\
D_{2222} &= E_2(1-\nu_{13}\nu_{31})\Upsilon, \\
D_{3333} &= E_3(1-\nu_{12}\nu_{21})\Upsilon, \\
D_{1122} &= E_1(\nu_{21}+\nu_{31}\nu_{23})\Upsilon = E_2(\nu_{12}+\nu_{32}\nu_{13})\Upsilon, \\
D_{1133} &= E_1(\nu_{31}+\nu_{21}\nu_{32})\Upsilon = E_3(\nu_{13}+\nu_{12}\nu_{23})\Upsilon, \\
D_{2233} &= E_2(\nu_{32}+\nu_{12}\nu_{31})\Upsilon = E_3(\nu_{23}+\nu_{21}\nu_{13})\Upsilon, \\
D_{1212} &= G_{12}, \\
D_{1313} &= G_{13}, \\
D_{2323} &= G_{23}, \\
\Upsilon &= \frac{1}{1-\nu_{12}\nu_{21}-\nu_{23}\nu_{32}-\nu_{31}\nu_{13}-2\nu_{21}\nu_{32}\nu_{13}}.
\end{aligned}$$

Equation 4: FEA software orthotropic stiffness matrix constant definitions

E11	**E22**	**E33**	**v12**	**v13**	**v23**
12852.4	12852.4	6434.74	0.121	0.117	0.117
G12	**G13**	**G23**			
3700	2900	2900			

Table 20: FR4 PWB Orthotropic Elastic Material Properties

Tables 21 and 22 provide the elastic isotropic material properties for the LCR ceramic body and the copper pads, respectively [57].

Density (10^3 kg/mm^3)	**Young's Modulus (MPa)**	**Poisson's Ratio**
1.2E-9	300000	0.3

Table 21: Ceramic body material properties

Density (10^3 kg/mm^3)	**Young's Modulus (MPa)**	**Poisson's Ratio**
8.9E-9	128000	0.35

Table 22: Copper pad material properties

Table 23 and Figure 44 provide the elastic and plastic isotropic properties for SAC305 solder, per data sets in Tables 7, 8. Material properties for data sets 3 and 4 are taken from the FE model properties of their respective studies in order to compare results (Chapter 5).

The cyclic fatigue curves extracted from vibration tests depend entirely on the stress-strain behavior assumed for the material, so fatigue models and stress-strain models should always be presented as paired properties. The solder strain values on the fatigue curves come from strain transfer functions produced through simulations, as discussed in Chapter 4. Each of these strain transfer functions depends on constitutive properties for SAC305 implemented in the FEA model.

Data Set # Per Tables 7, 8	**Density (10^3 kg/mm^3)**	**Young's Modulus (MPa)**	**Poisson's Ratio**
1a-c (20% pad LCR) 2 (20% pad LCR) 5 (20% pad LCR)	8.4E-9	62267.6	0.3
1a-c (100% pad LCR) 2 (100% pad LCR) 5 (100% pad LCR)	8.4E-9	54221.5	0.3
3	0 (quasi-static)	47500	0.3
4	0 (quasi-static)	46735.4	0.3

Table 23: SAC305 elastic material properties for Data Set 1a-c, 20% Pads

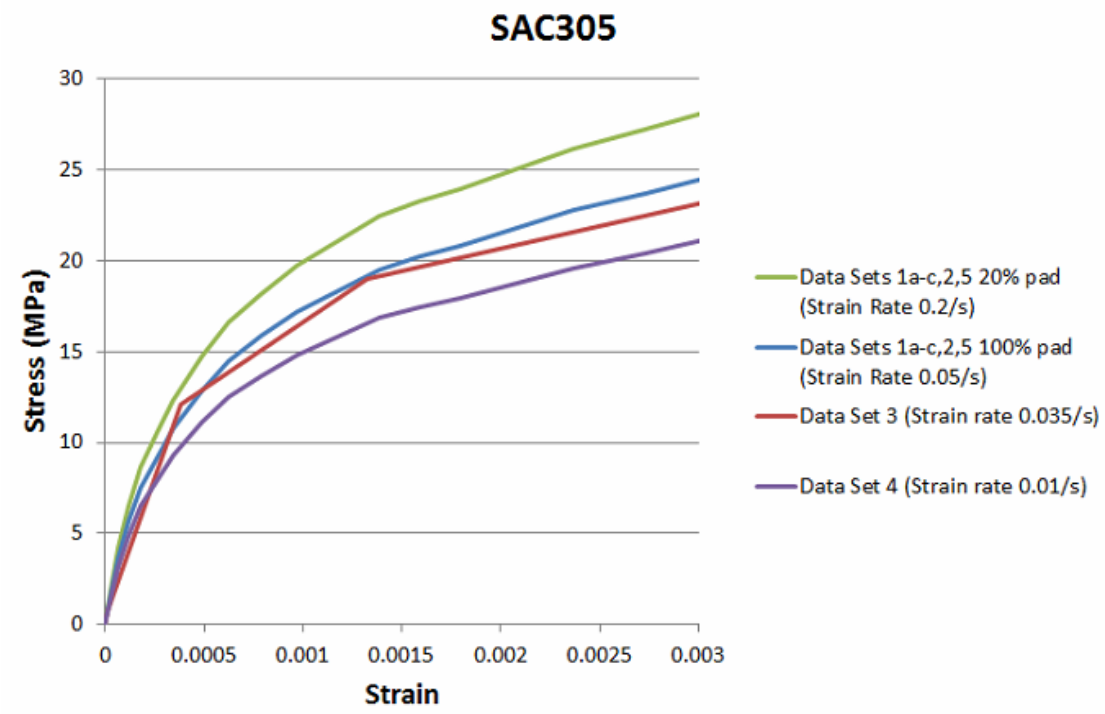

Figure 44: SAC305 stress strain curves for Data sets 1-5 of Tables 7, 8

Data sets 1a-c, 2, and 5 involve the PWA configuration used for this study. As stated in Chapter 4.2, estimates of the average strain rates of the tested specimens are 0.05/s for full (100%) pad specimens, and 0.2/s for narrow (20%) pad specimens. The base stress-strain curve from Data Set 4 (Figure 44) is scaled to these two strain rates using Cowper-Symonds parameters. The Cowper-Symonds model can be found in the form in Equation 5. An internal CALCE study [48] fitted data from Darveaux's stress-strain data for a low silver alloy, Sn1.2Ag0.5Cu0.05Ni, at high strain rates [49], and produced the model parameters in Figure 43.

$$\sigma = [A + B\epsilon_p^n]\left[1 + C\dot{\varepsilon}_p^m\right]$$

Equation 5: Cowper-Symonds Model

General model:
f(x,y) = (A+B*x^n)*(1+C*y^m)
Coefficients (with 95% confidence bounds):
A = 2.27 (-6.636, 11.18)
B = 10.83 (1.142, 20.52)
C = 2.903 (0.9153, 4.891)
m = 0.1482 (0.1153, 0.1812)
n = 0.1122 (-0.03302, 0.2574)

Goodness of fit:
SSE: 58.07
R-square: 0.9893
Adjusted R-square: 0.9879
RMSE: 1.391

Figure 45: Cowper-Symonds parameters from curve fitting tool results for SAC curves in [48]

Since only scaling of stress-strain curves is required, constants A, B, and n are not employed for this study. Constants for C and m were independently verified by fitting the low strain region of Darveaux's curves [49] to a power law model. Values were found to be within the 95% confidence bounds in Figure 43 for C and m.

The 0.05/s and 0.2/s SAC305 stress-strain curves, scaled by the Cowper-Symonds model, are based on estimates of average strain rate in the critical solder region; the actual average strain rates may differ. To obtain a constitutive model with more accurate representation of average solder strain rate, an iterative process is required. Each newly scaled stress-strain curve can be used to produce a new transfer function. Through the new transfer function, a new SAC strain range for the in-test PWB strain is obtained, which is then used to estimate a new strain rate. Strain rate estimates take into account the RMS strain range, the volume percent of the solder critical region in the entire solder fillet, and the frequency of the PWA response. The current SAC305 stress-strain curve is scaled to this new strain rate via Cowper-Symonds, implemented in the FEA model to produce yet another set of transfer

functions, which allow estimatation of yet another strain rate, etc. This iterative process can be repeated until the stress-strain curve converges to a stable solution. However, as discussed in Chapter 6.3.2 for future work, the more robust method is to implement the Cowper-Symonds model directly into the finite element model.

Alternate Material Properties: The Effect of Applied Stress-Strain Curves on Strain Transfer Functions and Fatigue Curves

As emphasized in Chapters 4 and 6, the analysis methods used in this study require careful consideration when applying SAC305 material properties. The applied stress-strain curves must be paired with the resulting strain transfer functions and fatigue curves. Alterations in the SAC properties result in different strain transfer functions, and thus different fatigue curves.

The material fatigue curves presented in Figure 44 for Data sets 1a-c, 2, and 5 are based on Darveaux's constitutive model for SAC305, published in 1992 [49]. Darveaux has since updated his stress-strain curves for SAC305 in a newer (2005) study, for joint specimens aged 24 hours at 125°C [58], copied below in Figure 46. The desired strain rates for full and narrow pads (0.05/s and 0.2/s, respectively) can be obtained by scaling to 0.01/s and 0.1/s stress-strain curves, respectively. By fitting a power law model to the stress-strain data at different strain rates (Figure 46), Cowper-Symonds parameters C (0.83) and m (0.11) in Equation 5 are extracted. An elastic modulus (47.5 GPa) is obtained from Darveaux's original constitutive model in [49] for 25°C. The resulting scaled stress-strain curves are presented in Figure 47. However, the constitutive model for SAC305 in [49] is largely inconsistent with the curves produced in [58], as seen in Figure 47, maybe due to modified testing

methods. So, although there is newer data available, the 2005 stress-strain curves are not employed since they are pieced together from separate, inconsistent sources [49, 58]. Since [49] contains a complete constitutive model, it is used as the base curve for application of the Cowper-Symonds model.

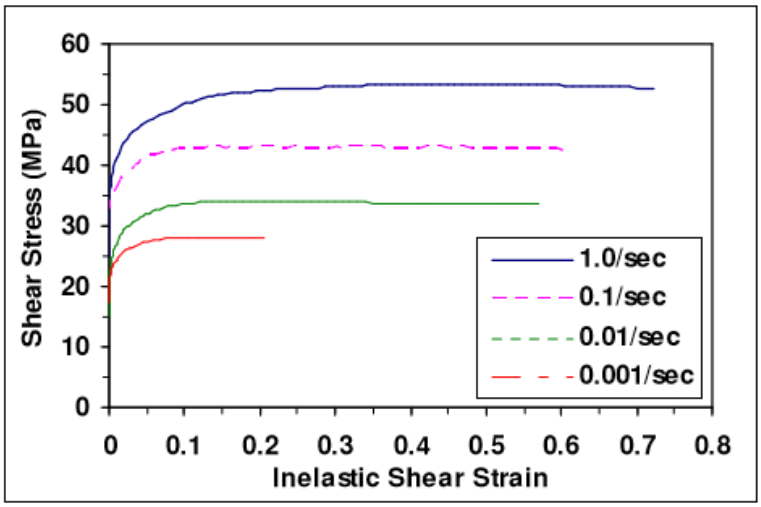

Figure 46: SAC305 shear stress-strain curve for specimens aged 24 hrs @ 125°C [58]

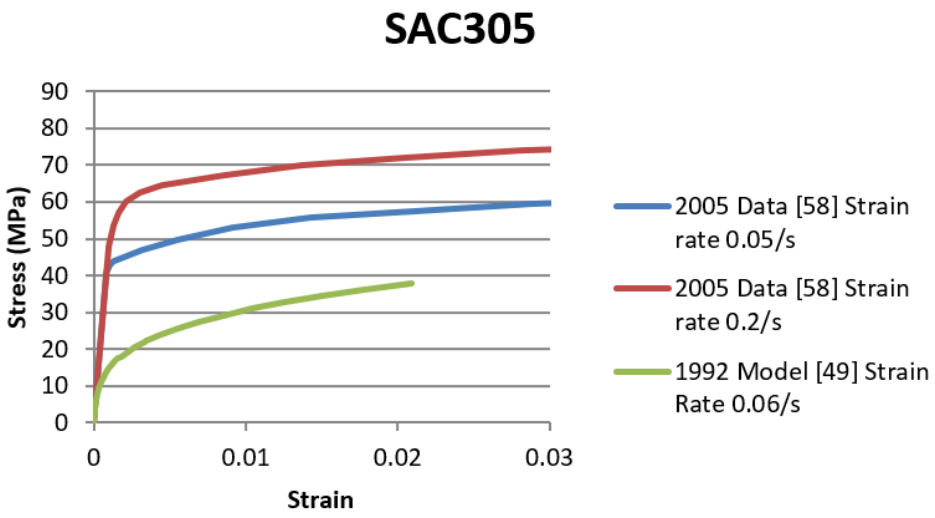

Figure 47: SAC305 scaled stress-strain curves (0.05/s, 0.2/s) based on data in [58], and an unscaled stress-strain curve (0.06/s) from the constitutive model in [49]

The strain transfer functions produced from the curves in Figure 47 (strain rates 0.05/s, 0.2/s) are below, in Figure 48. The functions for both full and narrow pads are very linear, since strains in the solder did not surpass the elastic region of the stress-strain curve.

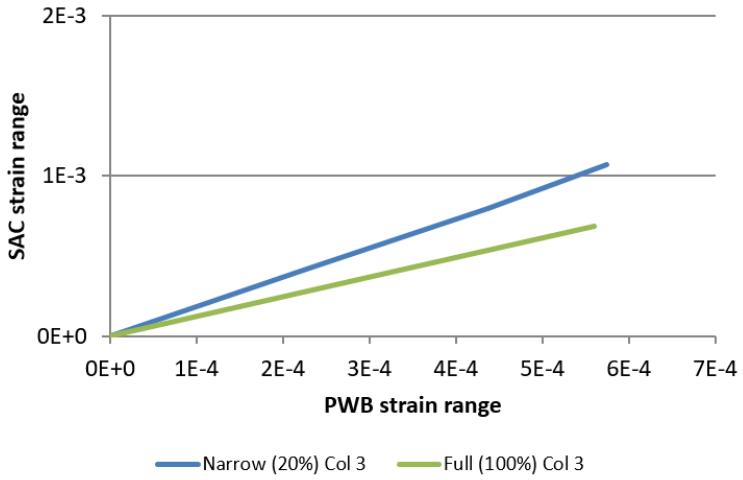

Figure 48: Strain transfer functions for SAC305 material properties in Figure 47

The resulting fatigue curves as a function of high temperature aging duration (Figure 49) and as a function of surface finish and room temperature aging (Figure 50) are different from those presented in Chapter 6, due to the change in SAC305 material properties, and thus a change in the strain transfer functions. The slopes of the curves have remained stable in this case, but the magnitudes of the solder strains have decreased. This further highlights the importance of applying material properties and fatigue curves as paired properties, when designing with these material curves.

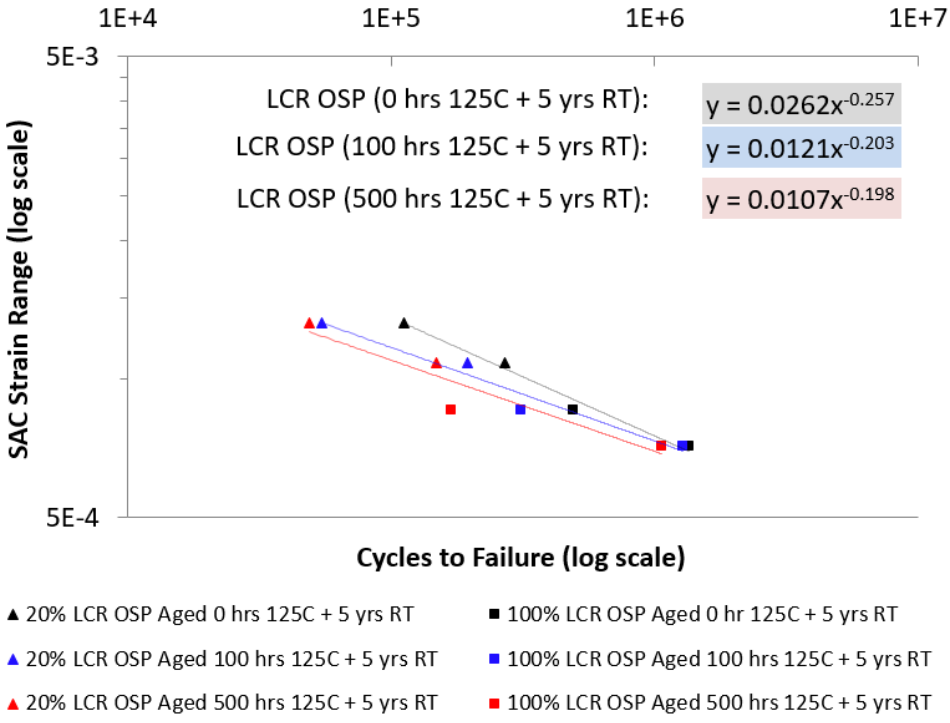

Figure 49: (Using stress-strain properties in Figure 47) SAC305/OSP fatigue curves as a function of high temperature aging (Data sets 1a-c per Table 7)

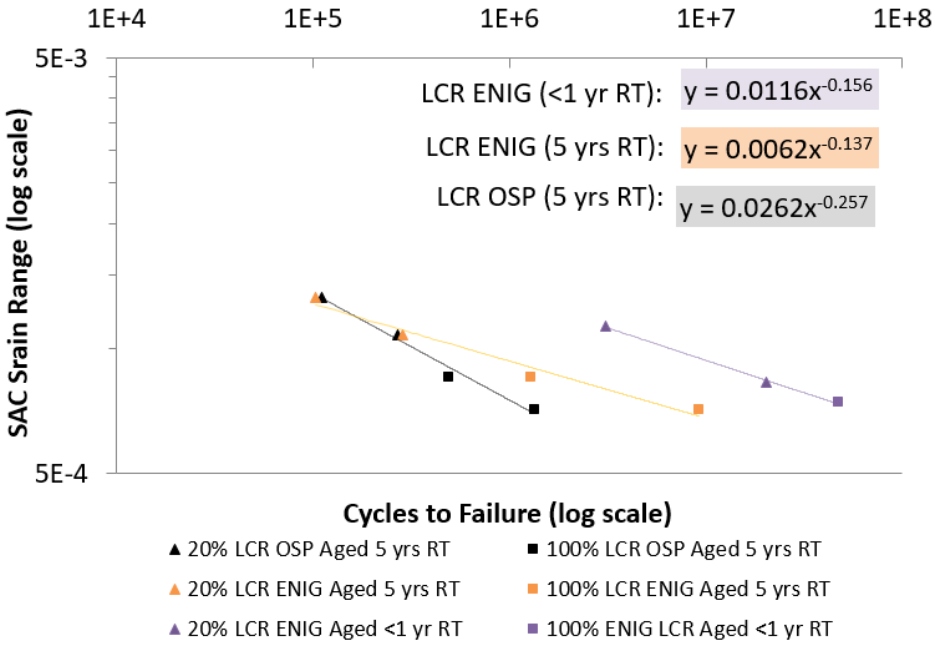

Figure 50: (Using stress-strain properties in Figure 47) SAC305/OSP, SAC305/ENIG fatigue curves for no additional aging beyond storage (Data sets 1a, 2, 5 per Tables 7, 8)

A.2 Failure Analysis Cross-sections

Selected early and mid-late failures in data sets 1a-c of Table 7 are cross-sectioned and imaged via E-SEM. A summary of failure sites is tabulated in Table 24, corresponding to Figures 51-59.

Early Failures	**Failure Sites**	**Figure**
Aged 0 hrs	Solder (R28)	51
Aged 100 hrs	Solder (R33)	52
Aged 500 hrs	Solder + Trace (R3)	53, 54
Mid-Late Failures	**Failure Sites**	**Figure**
Aged 0 hrs	Solder + Trace (R17)	55
	Trace (R27)	56
Aged 100 hrs	Solder (R24)	57
	Trace (R14)	58
Aged 500 hrs	Trace (R22)	59

Table 24: Failure sites for selected early and mid-late failures

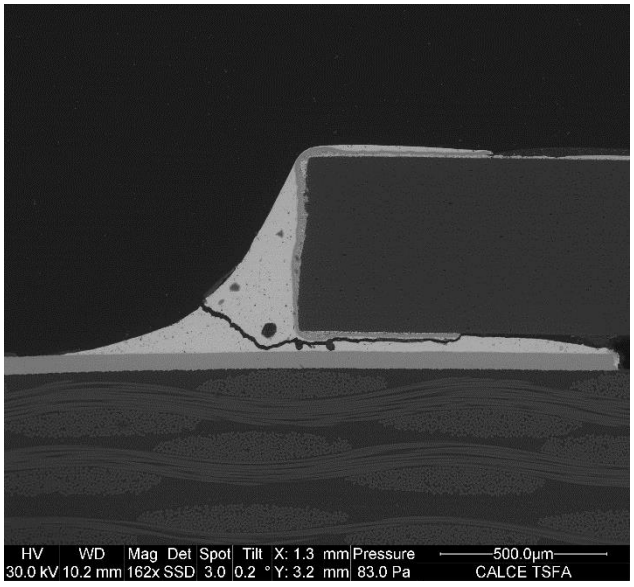

Figure 51: Solder Crack in R28 (Aged 0 Hours, Early Failure)

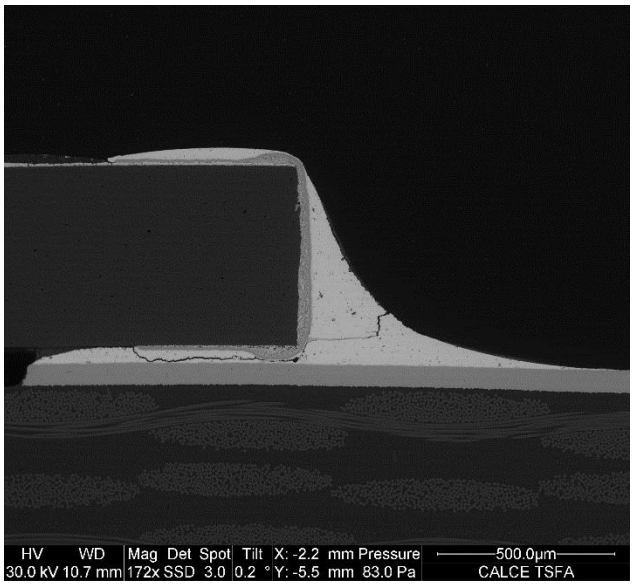

Figure 52: Solder Crack in R33 (Aged 100 Hours, Early Failure)

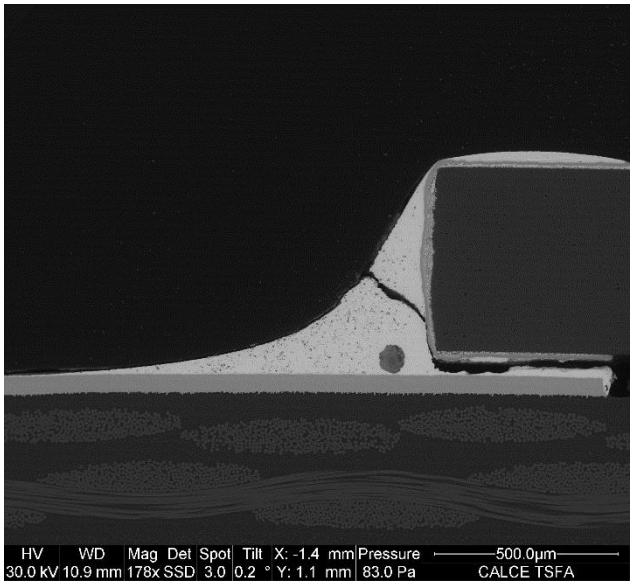

Figure 53: Solder Crack in R3 (Aged 500 Hours, Early Failure)

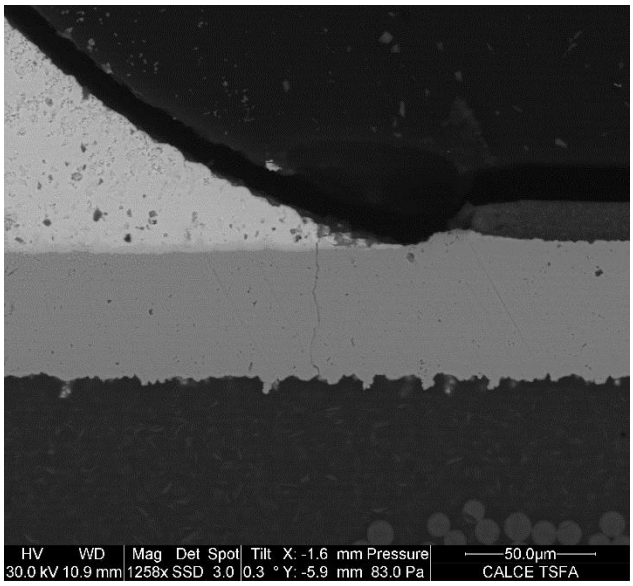

Figure 54: Trace Crack in R3 (Aged 500 Hours, Early Failure)

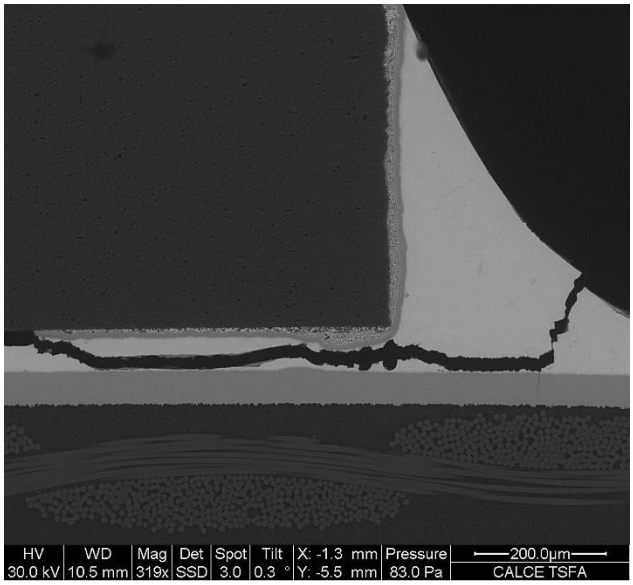

Figure 55: Solder and Trace Crack in R17 (Aged 0 Hours, Mid-Late Failure)

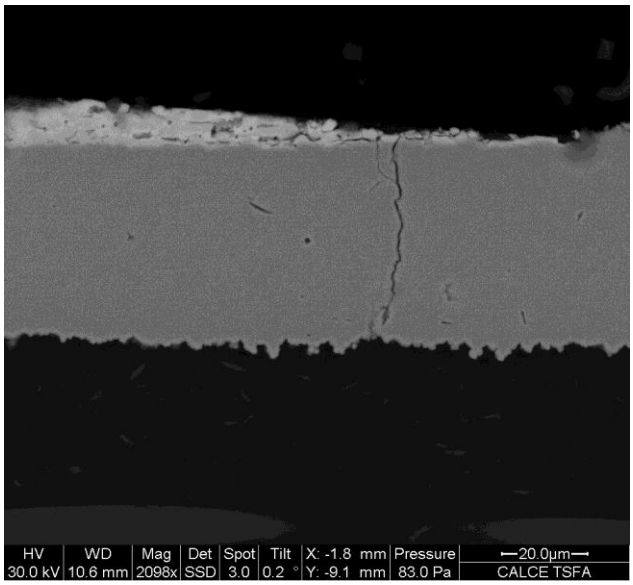

Figure 56: Trace Crack in R27 (Aged 0 Hours, Mid-Late Failure)

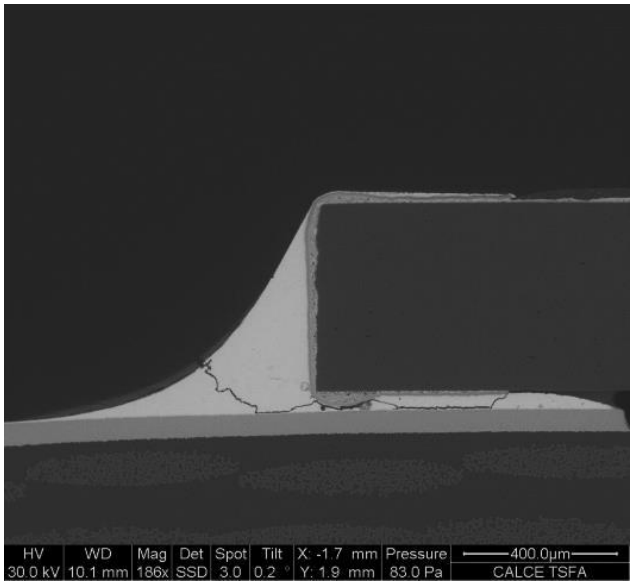

Figure 57: Solder Crack in R24 (Aged 100 Hours, Mid-Late Failure)

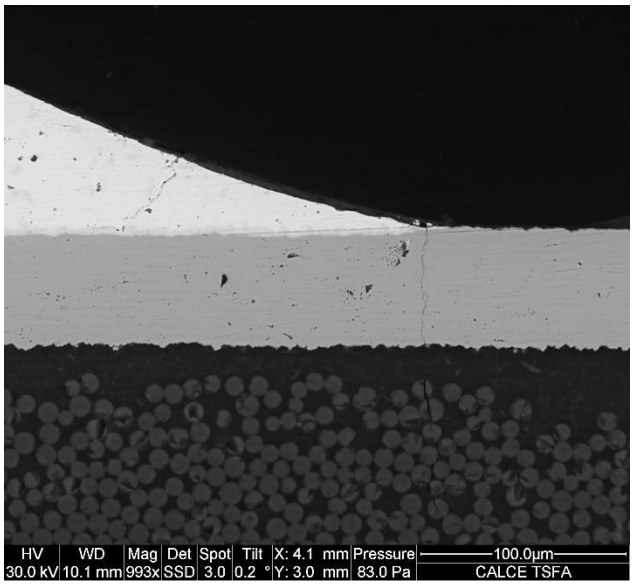

Figure 58: Trace Crack in R14 (Aged 100 Hours, Mid-Late Failure)

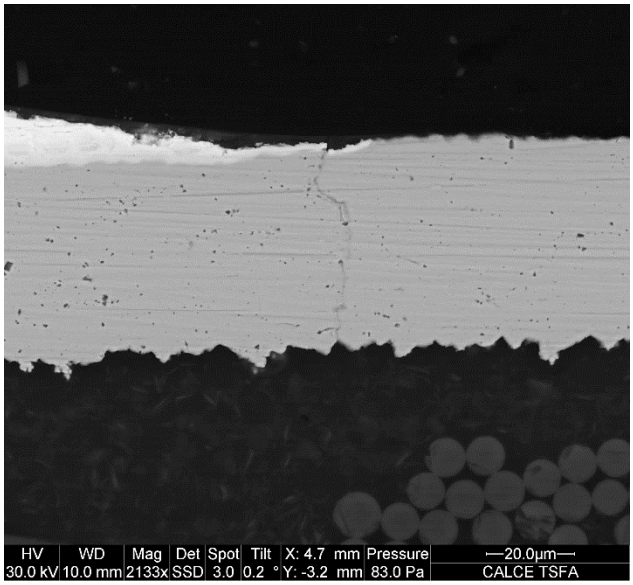

Figure 59: Trace Crack in R22 (Aged 500 Hours, Mid-Late Failure)

A.3 Weibull Analysis Plots

SAC305/OSP Weibull Plots

A summary of Weibull Parameters, extracted from the tests results and used for the SAC305/OSP S-N curves in Figure 38 (Data sets 1a-c in Table 7), is presented in Table 15. Weibull plots for each stress level are in Figures 60 through 63. The legend for all plots is as follows: Aged 0 hours (Black circle), Aged 100 hours (Blue upright triangle), Aged 500 hours (Red upside down triangle). These aging times refer to additional aging of the PWAs at 125°C, after 5 years of room temperature storage.

SAC305/OSP	Aging Time @ 125°C (Hours)	Shape Parameter Beta (β)	Scale Parameter Eta (η)
Col 3 Narrow (20%) Pad	0	3.56	111834
	100	11.7	54800
	500	7.09	48830
Col 2, 4 Narrow (20%)Pad	0	1.89	270575
	100	2.17	195075
	500	2.88	148312
Col 3 Full (100%) Pad	0	3.56	111834
	100	11.7	54800
	500	7.09	48830
Col 2, 4 Full (100%) Pad	0	2.85	489933
	100	4.52	311972
	500	11.0	169735

Table 25: Two-parameter Weibull parameters for unscaled failure data (SAC305/OSP)

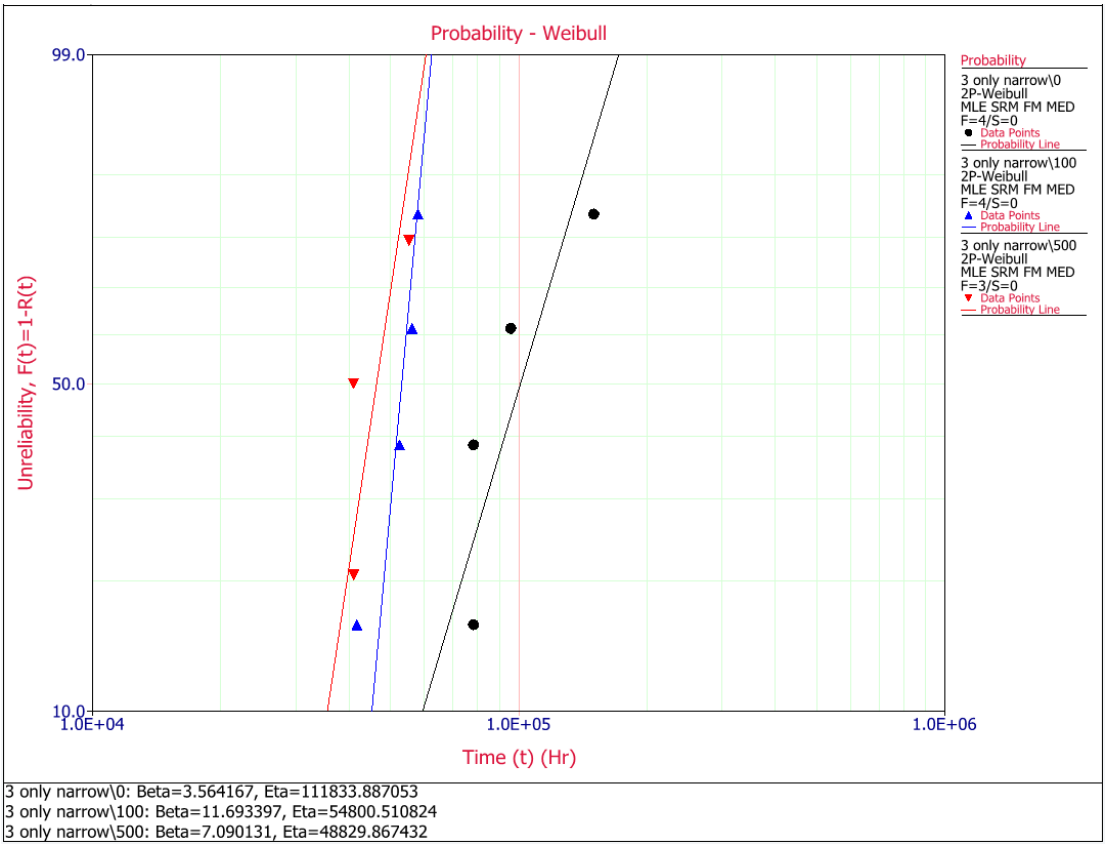

Figure 60: Two-parameter Weibull plots for Col 3 narrow (20%) pad failures (SAC305/OSP)

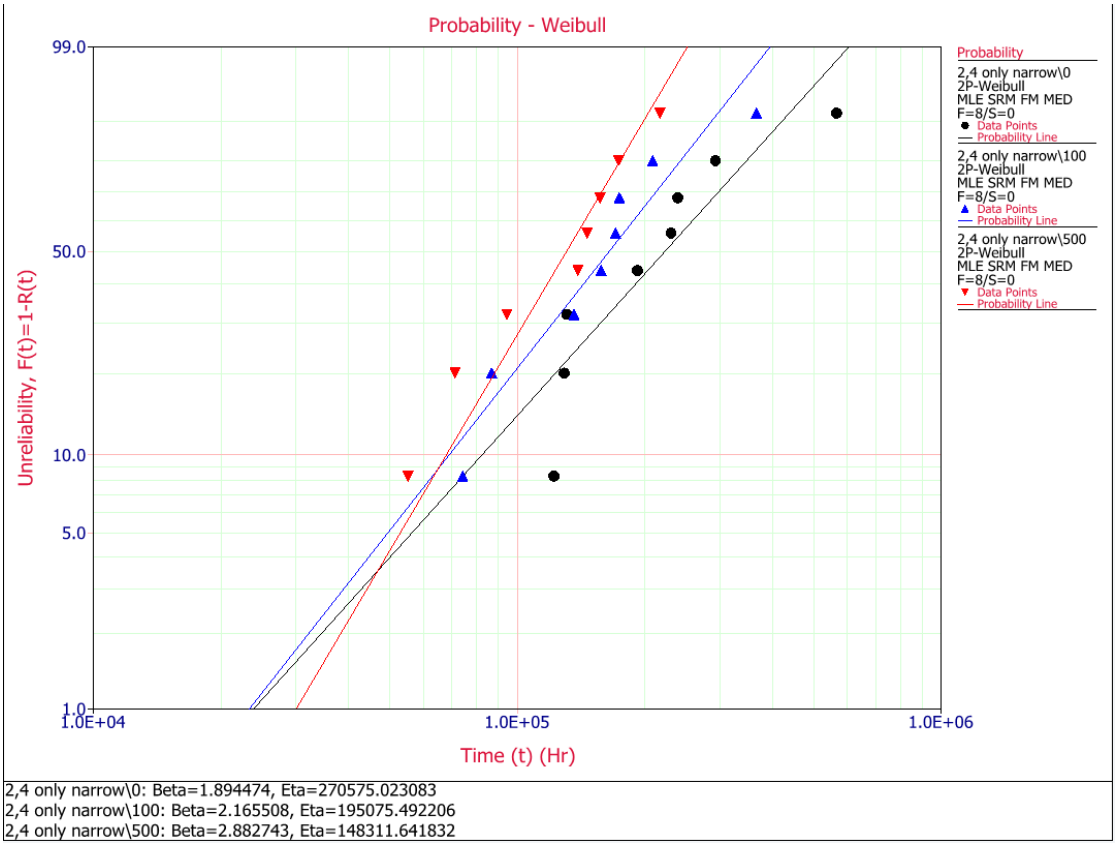

Figure 61: Two-parameter Weibull plots for Col 2, 4 narrow (20%) pad failures (SAC305/OSP)

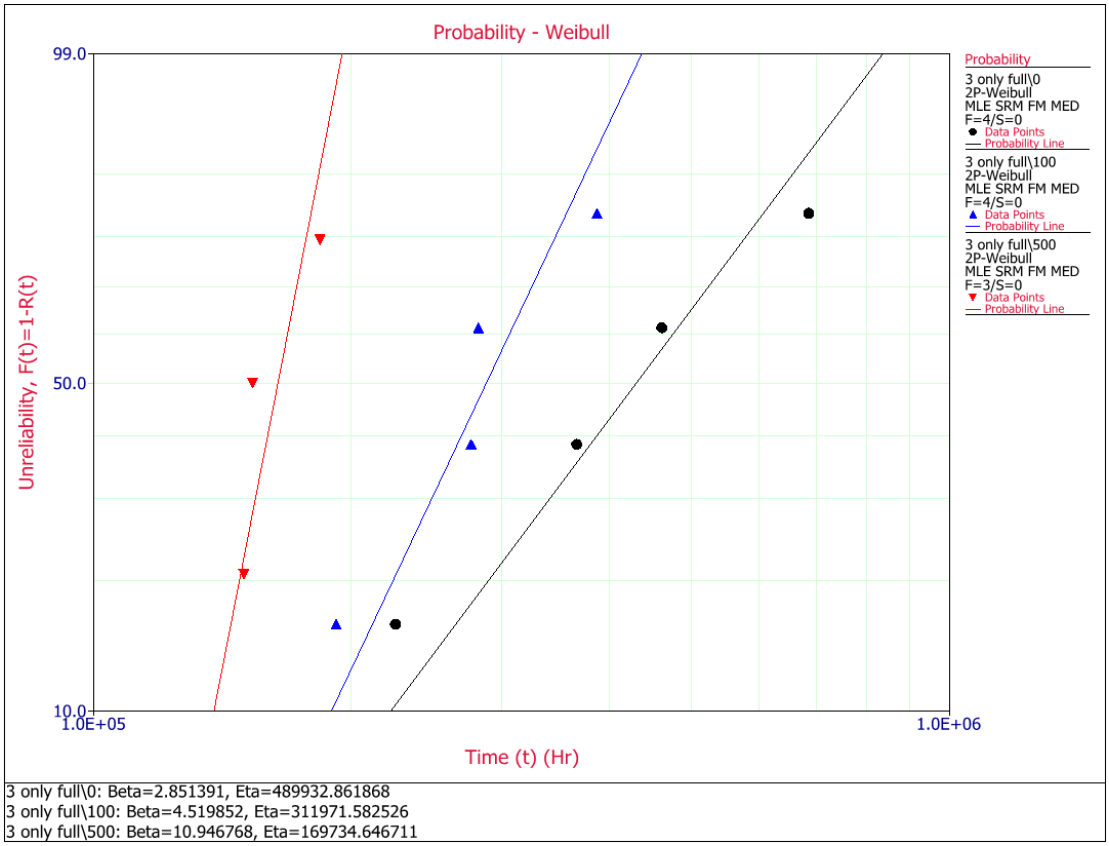

Figure 62: Two-parameter Weibull plots for Col 3 full (100%) pad failures (SAC305/OSP)

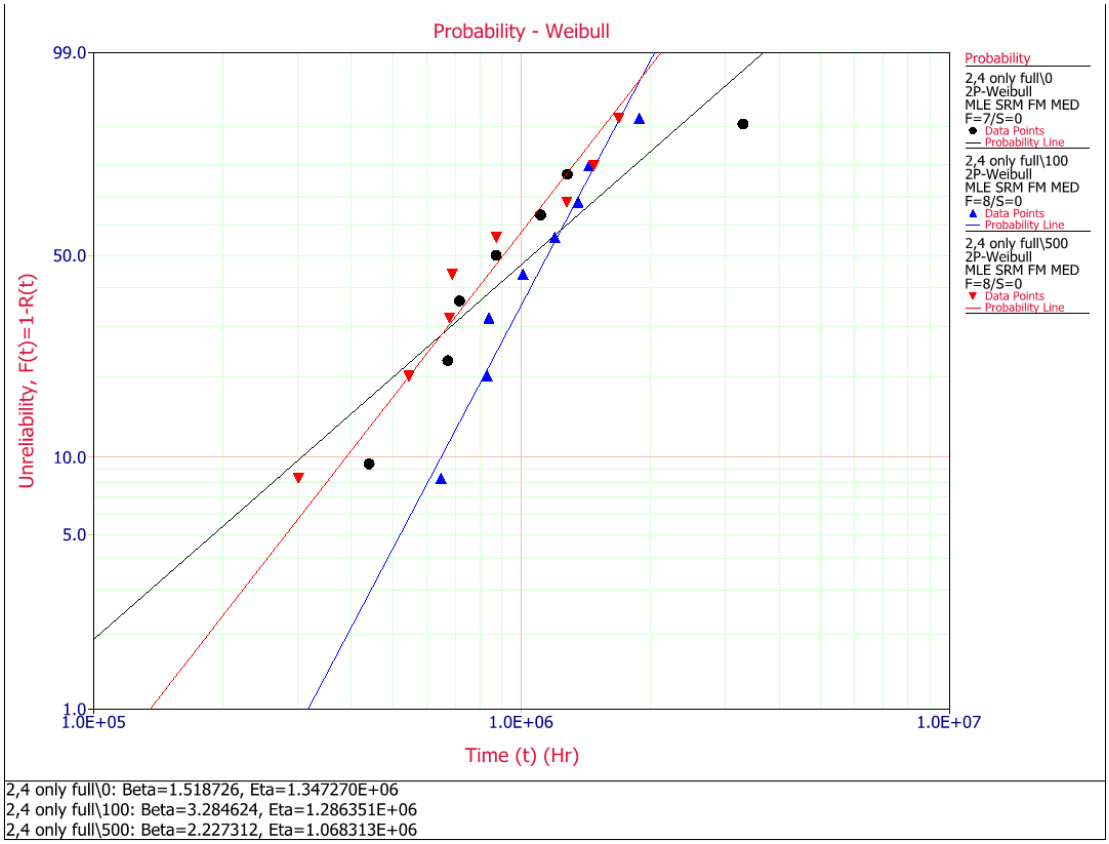

Figure 63: Two-parameter Weibull plots for Col 2, 4 full (100%) pad failures (SAC305/OSP)

SAC305/OSP: Raw Failure Data for Each Stress Grouping

Some failure data points were not included in the analysis, namely: LCRs which did not record failures (highlighted in yellow in Tables 26-28), and those which failed by a large manufacturing void (red text in Table 28). Ideally the data set would be comprised entirely of solder crack failures, however trace crack failures remain in the data set. Trace cracks are a highly likely failure mode, and are largely prevalent in the lower stress level failures. It is extremely time-consuming to segregate lower stress level failures into solder and trace cracks. Thus, trace crack failures identified through failure analysis remain in the data set. Large void manufacturing defects, however, lead to abnormal stress concentrators in the solder, resulting in its appearance in late outlier failures. Because it is likely that void-related failures were identified in the outlier failures cross-sectioned, and that their percentage of occurrence is small relative to trace cracks, void-related failures are removed from the data set. The component and void defect in question is shown in Figure 64.

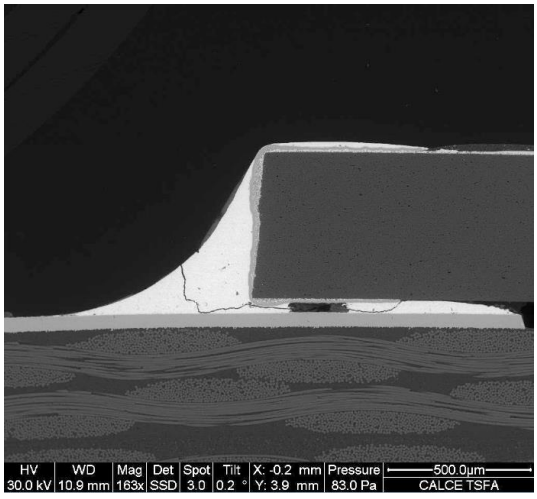

Figure 64: Void defect in joint

20% Col 3	20% Col 2,4	100% Col 3	100% Col 2,4
78400	122150	225400	440650
78400	129150	367150	673400
95900	130900	461650	717150
150150	192150	685650	872900
	230650		1109500
	239400		1281000
	293650		3298750
	566650		

Table 26: Raw failure data for SAC305/OSP PWA Aged 0 hours @ 125C + 5 years room temperature storage

20% Col 3	20% Col 2,4	100% Col 3	100% Col 2,4
41745	74415	192150	649650
52635	87120	276330	832650
56265	136125	281820	839970
58080	157905	387960	1010160
	170610		1198650
	174240		1357860
	208725		1440210
	366630		1886730

Table 27: Raw failure data for SAC305/OSP PWA Aged 100 hours @ 125C + 5 years room temperature storage

20% Col 3	20% Col 2,4	100% Col 3	100% Col 2,4
41032	55304	149856	301344
41032	71360	153424	546624
55304	94552	183960	679776
1692432	139152		690288
	146288		874248
	156992		1277208
	173448		1476936
	217248		1692432

Table 28: Raw failure data for SAC305/OSP PWA Aged 500 hours @ 125C + 5 years room temperature storage

SAC305/ENIG Weibull Plots

A summary of Weibull Parameters, used for the SAC305/ENIG S-N curves in Figure 39 (Data set 2 in Table 7), is presented in Table 29. One data point is censored (no failure recorded). Weibull plots for each stress level are in Figures 65 through 68. The PWA was not aged additionally after 5 years of room temperature storage.

SAC305/ENIG	Shape Parameter Beta (β)	Scale Parameter Eta (η)
Col 3 Narrow (20%) Pad	1.24	103774
Col 2, 4 Narrow (20%) Pad	2.28	288431
Col 3 Full (100%) Pad	1.89	1.29E6
Col 2, 4 Full (100%) Pad	1.51	9.17E6

Table 29: Two-parameter Weibull parameters for unscaled failure data (SAC305/ENIG)

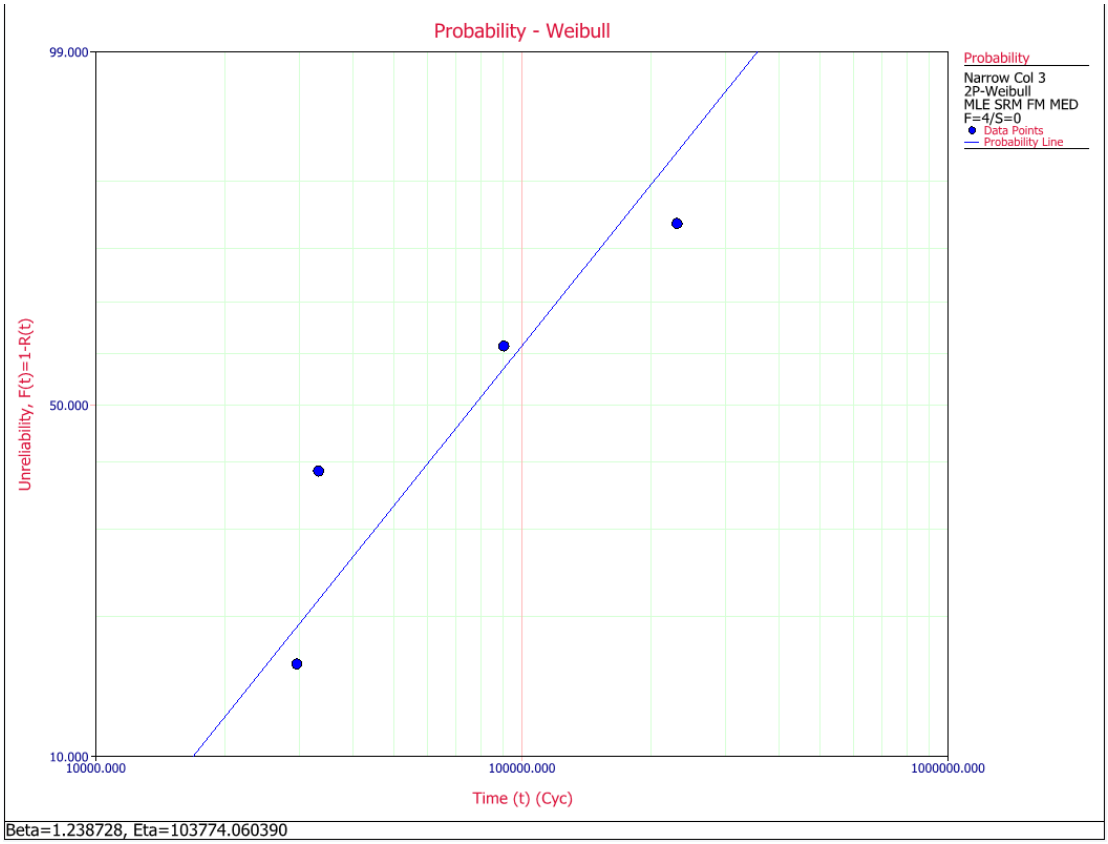

Figure 65: Two-parameter Weibull plots for Col 3 narrow (20%) pad failures (SAC305/ENIG)

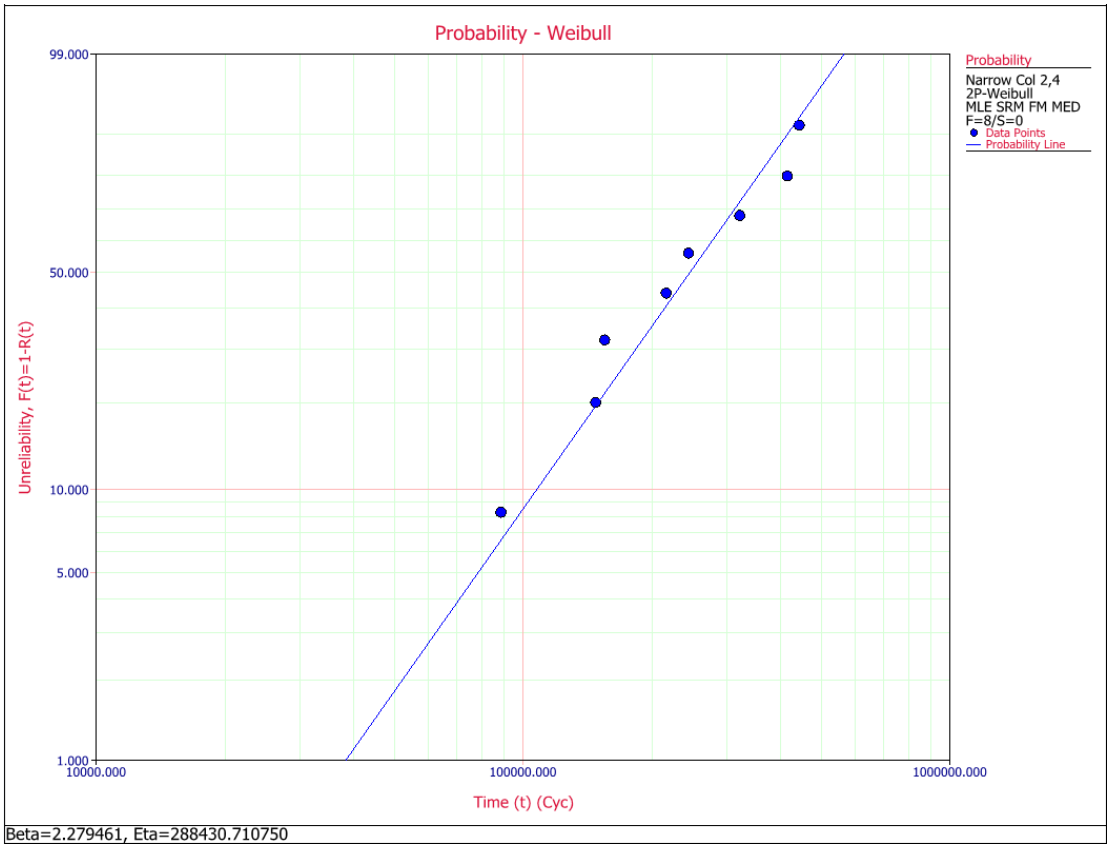

Figure 66: Two-parameter Weibull plots for Col 2, 4 narrow (20%) pad failures (SAC305/ENIG)

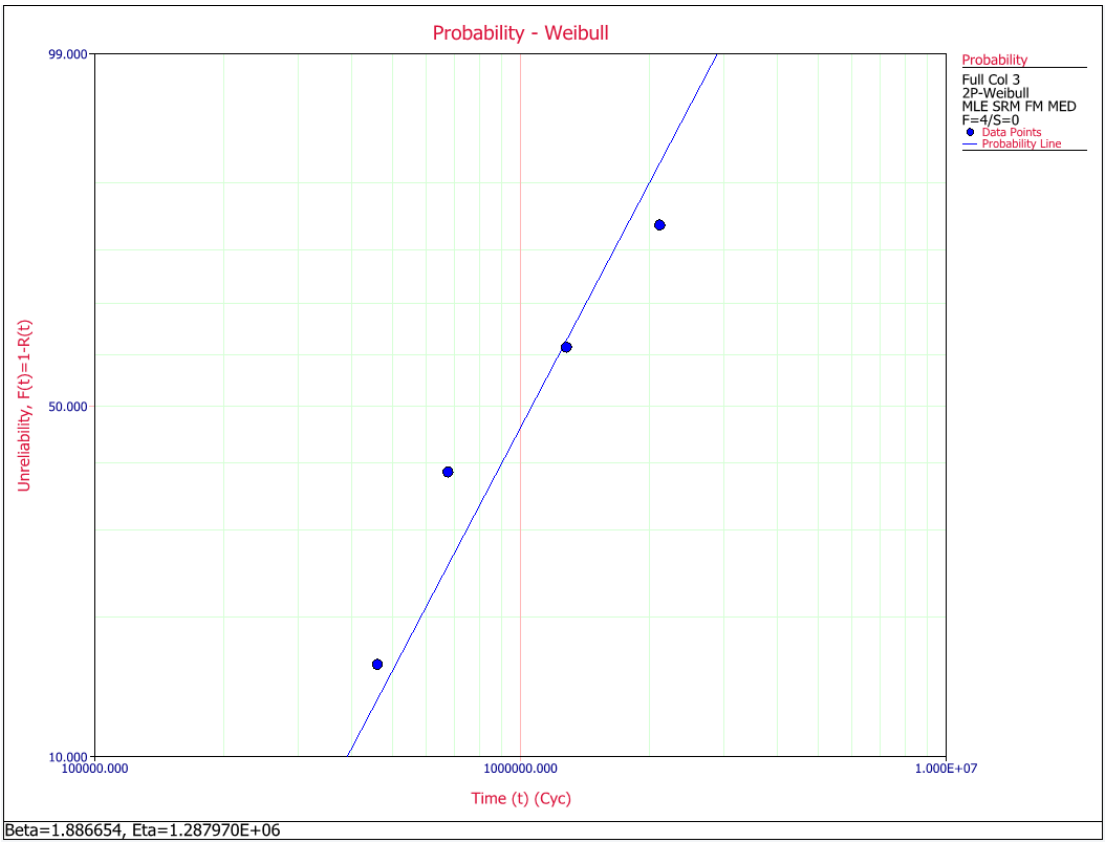

Figure 67: Two-parameter Weibull plots for Col 3 full (100%) pad failures (SAC305/ENIG)

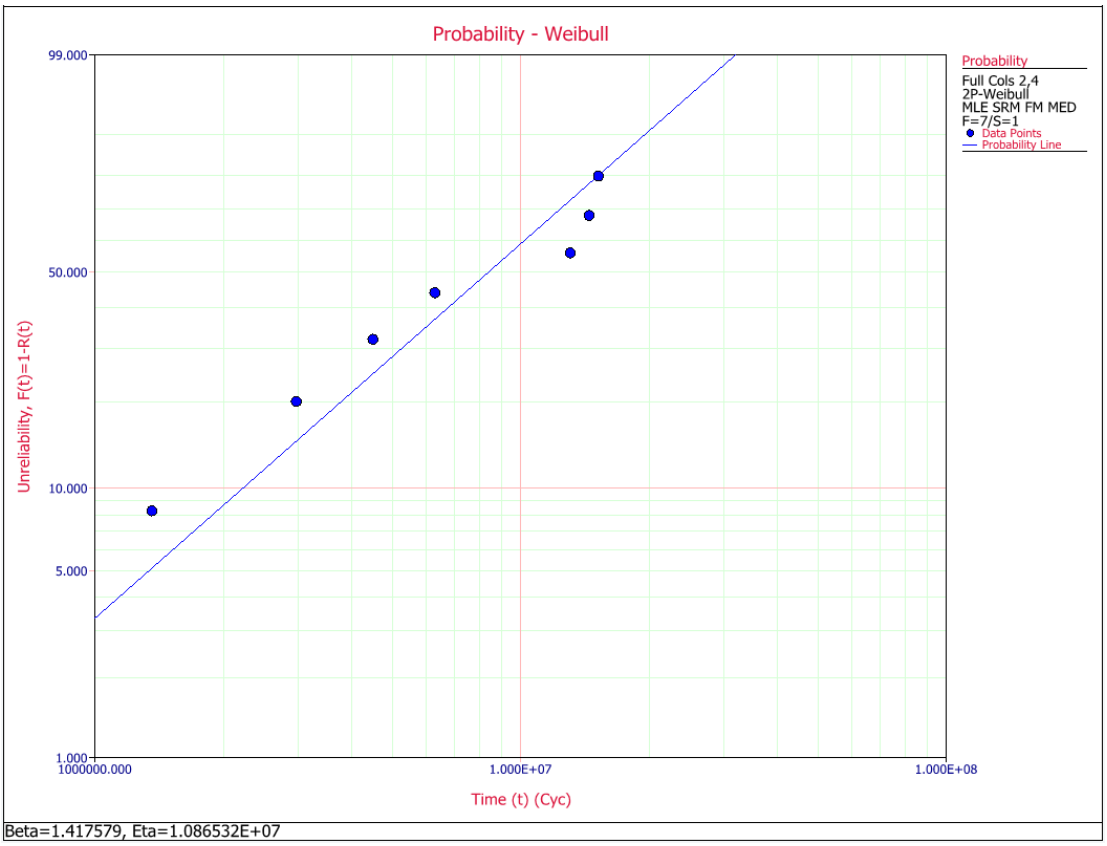

Figure 68: Two-parameter Weibull plots for Col 2, 4 full (100%) pad failures (SAC305/ENIG)

SAC305/ENIG: Raw Failure Data for Each Stress Grouping

The raw failure data for the SAC305/ENIG PWA is in Table 30. Unfailed specimens excluded from the analysis are highlighted in yellow.

20% Col 3	20% Col 2,4	100% Col 3	100% Col 2,4
29600	88800	460650	1361600
33300	148000	675250	2974800
90650	155400	1282050	4501050
231250	216450	2123800	6290000
	244200		13092450
	321900		14494750
	416250		15247700
	444000		

Table 30: Raw failure data for SAC305/ENIG PWA Aged 5 years in room temperature storage

References

[1] "Directive on Waste of Electronic Equipment (WEEE)," 2001.

[2] “Lead-free Electronics in Aerospace Systems,” Boeing Phantom Works, Engineering, Operations & Technology, Parts Standardization and Management Committee, 2006.

[3] "Performance Test Methods and Qualification Requirements for Surface Mount Solder Attachments," IPC-9701A, 2006.

[4] M. Motolab, Z. Cai, J. Suhling, J. Zhang, J. Evans, M. Bozack, and P. Lall, “Improved Predictions of Lead Free Solder Joint Reliability that Include Aging Effects,” in Proceedings of the Electronic Components and Technology Conference, 2012.

[5] P. Chauhan, S. Mukherjee, M. Osterman, A. Dasgupta, and M. Pecht, “Effect of Isothermal Aging on Microstructure and Creep Properties of SAC305 Solder – A Micromechanics Approach,” Proceedings of the ASME International Technical Conference and Exhibition on Packaging and Integration of Electronic and Microsystems (InterPACK), 2013.

[6] Y. Zhang, Z. Cai, J, Suhling, and P. Lall, “The Effects of Aging on the Mechanical Behavior of Lead Free and Mixed Formulation Solder Alloys,” Ph.D., Auburn University, 2010.

[7] S. Wiese, M. Roellig, and K.J. Wolter, “Creep of Thermally Aged SnAgCu-Solder Joints,” 6th International Conference on Thermal, Mechanical, and Multiphysics Simulation and Experiments in Micro-Electronics and Micro-Systems, EuroSimE, 2005.

[8] Q. Xiao, L. Nguyen, and W. Armstrong, "Aging and Creep Behavior of Sn3.9Ag0.6Cu Solder Alloy," Electronic Components and Technology Conference, 2004.

[9] A. R. Fix, W. Nuchter, and J. Wilde, "Microstructural Changes of Lead-free Solder Joints During Long-term Ageing, Thermal Cycling, and Vibration Fatigue," Soldering & Surface Mount Technology, vol. 20, no. 1, pp. 13-21, 2008.

[10] I. Dutta, P. Kumar, and G. Subbarayan, "Microstructural Coarsening in Sn-Ag-based Solders and its Effects on Mechanical Properties," Journal of the Minerals, Metals, & Materials Society, vol. 61, no. 6, pp. 29-38, 2009.

[11] C. Morando, O. Fornaro, O. Garbellini, H. Palacio, "Microstructure evolution during the aging at elevated temperature of Sn-Ag-Cu solder alloys," 11th International Congress on Metallurgy & Materials (SAM/CONAMET), 2011.

[12] B. S. S. Rao, J. Weng, L. Shen, T. K. Lee, K. Y. Zeng, "Morphology and Mechanical Properties of Intermetallic Compounds in SnAgCu Solder Joints," Microelectronic Engineering, vol. 87, no. 11, pp. 2416-2422, 2010.

[13] P. Chauhan, M. Osterman, and M. Pecht, "Impact of Thermal Aging on the Growth of Cu-Sn Intermetallic Compounds in Pb-free Solder Joints in 2512 Resistors," Proceedings of the ASME 2009 International Mechanical Engineering Congress & Exposition (IMECE), 2009.

[14] A. Choubey, H. Yu, M. Osterman, M. Pecht, F. Yun, L. Yonghong, and X. Ming, "Intermetallics Characterization of Lead-free Solder Joints under Isothermal Aging," Journal of Electronic Materials, vol. 37, no. 8, 2008.

[15] K. Sinha, J. Varghese, and A. Dasgupta, “Effect of Geometric Complexities and Nonlinear Material Properties on Interfacial Crack Behavior in Electronic Devices,” Microelectronics Reliability, vol. 54, pp. 610-618, 2014.

[16] L. Xu and J. H. L. Pang, “Effect of Intermetallic and Kirkendall Voids Growth on Board Level Drop Reliability for SnAgCu Lead-free BGA Solder Joint,” Proceedings of the 56th Electronic Components and Technology Conference, 2006.

[17] J. W. Jang, J. K. Lin, and D. R. Frear, “Failure Morphology after the Drop Impact Test of the Ball Grid Array Package with Lead-Free Sn-3.8Ag-0.7Cu on Cu and Ni Under-Bump Metallurgies,” Journal of Electronic Materials, vol. 36, no. 3, 2007.

[18] J. Varghese, A. Dasgupta, B. Song, M. Azarian, and M. Pecht, “The Role of Aging on Dynamic Failure Envelopes of OSP-Sn37Pb Interconnects in Plastic Ball Grid Array (PBGA) Packages,” IEEE Transactions on Components and Packaging Technologies, vol. 32, no. 1, 2009.

[19] R. Pratt, E. I. Stromswold, and D. J. Quesnel, “Effect of Solid-State Intermetallic Growth on the Fracture Toughness of Cu/63Sn-37Pb Solder Joints,” IEEE Transactions on Components, Packaging, and Manufacturing Technology – Part A, vol. 19, no. 1, 1996.

[20] M. Powers, J. Pan, J. Silk, P. Hyland, “Effect of Gold Content on the Microstructural Evolution of SAC305 Solder Joints Under Isothermal Aging,” Journal of Electronic Materials, vol. 41, no. 2, pp. 224, 2012.

[21] H. Ma, J. Suhling, P. Lall, M. Bozack “Reliability of the aging lead free solder joint,” in Proceedings of the 56th Electronic Components and Technology Conference, 2006.

[22] N. Vijayakumar, S. Thirugnanasamanbandam, P. Soobramaney, J. Zhang, T. Sanders, J. Evans, G. Flowers, M. Bozack, "The Effect of Isothermal Aging on Vibrational Performance of SAC105 and 305 Alloys," in Proceedings of the IEEE International Symposium on Advanced Packaging Materials, 2013.

[23] H. Qi, G. Plaza, S. Ganesan, M. Osterman, and M. Pecht, “Reliability Assessment on Insertion Mount Assembly under Vibration Conditions,” Electronic Components and Technology Conference, 2007.

[24] Y. Zhou, G. Plaza, A. Dasgupta, and M. Osterman, “Vibration Durability of Sn3.0Ag0.5Cu (SAC305) Solder Interconnects: Harmonic and Random Excitation,” Journal of the Institute of Environmental Sciences and Technology (IEST), vol. 52, no.1, pp.63-86, 2009.

[25] Y. Zhou, M. Al-Bassyiouni, and A. Dasgupta, “Vibration Durability Assessment of Sn3.0Ag0.5Cu and Sn37Pb Solders Under Harmonic Excitation,” Journal of Electronic Packaging, vol. 131, no. 1, 2009.

[26] C. Choi, M. Al-Bassyiouni, and A. Dasgupta, "Vibration Durability of Pb-free HVQFN Asssemblies," Proceedings of the 11th International Conference on Thermal, Mechanical, and Multiphysics Simulation and Experiments in Micro-Electronics and Micro-Systems, 2010.

[27] B. M. Paquette and D. B. Barker, “Harmonic Vibration Testing of Electronic Components Attached to Printed Wiring Boards with SAC305 and Eutectic SnPb Solder,” M.S., University of Maryland College Park, 2010.

[28] S. Menon, A. Pearl, M. Osterman, M. Pecht, "Effect of ENEPIG Surface Finish on the Vibration Durability of Solder Interconnects," in Proceedings of the IMAPS International Symposium on Microelectronics Conference, 2013.

[29] P. Matkowski and J. Felba, “Influence of Solder Joint Constitution and Aging Process Duration on Reliability of Lead-Free Solder Joints under Vibrations Combined with Thermal Cycling”

[30] J. Pan, J. Silk, M. Powers, P. Hyland, “Effect of Gold Content on the Reliability of SnAgCu Solder Joints,” IEEE Transactions on Components, Packaging and Manufacturing Technology, 2011.

[31] O. H. Basquin, "The Exponential Law of Endurance Tests," in Proceedings of the American Society for Testing and Materials, vol. 10, pp. 625-630, 1910.

[32] L. F. Coffin, "A Study of the Effects of Cyclic Thermal Stresses on a Ductile Metal," Transactions of the ASME, vol. 76, pp. 931-950, 1954.

[33] S. S. Manson, "Behavior of Materials Under Conditions of Thermal Stress," National Advisory Committee on Aeronautics Report, no. 1170, 1954.

[34] N. E. Dowling, "Mechanical Behavior of Materials," Prentice-Hall International, New Jersey, 1993.

[35] T. Eckert, M. Kruger, W. H. Muller, N. F. Nissen, and H. Reichl, “Investigation of the Solder Joint Fatigue Life in Combined Vibration and

Thermal Cycling Tests," Electronic Components and Technology Conference, 2010.

[36] K. Meier, M. Roellig, A. Schiessl, K. Wolter, "Reliability Study on Chip Capacitor Solder Joints under Thermo-Mechanical and Vibration Loading," 15th International Conference on Thermal, Mechanical, and Multi-Physics Simulation and Experiments in Microelectronics and Microsystems (EuroSimE), 2014.

[37] K. Upadhyayula and A. Dasgupta "An incremental damage superposition approach for reliability of electronic interconnects under combined accelerated stresses," The American Society of Mechanical Engineers, 1997.

[38] D. Yu, A. Al-Yafawi, T. T. Nguyen, S. Park, S. Chung, "High-cycle Fatigue Life Prediction for Pb-free BGA under Random Vibration Loading," Microelectronics Reliability, no. 51, pp. 649-656, 2011.

[39] T. E. Wong, F. W. Palmieri, B. A. Reed, H. S. Fenger, H. M. Cohen, and K. T. Teshiba, "Durability/Reliability of BGA Solder Joints under Vibration Environment," Electronic Components and Technology Conference, 2000.

[40] S. F. Wong, P. Malatkar, C. Rick, V. Kulkarni, I. Chin, "Vibration Testing and Analysis of Ball Grid Array Package Solder Joints," Electronic Components and Technology Conference, 2007.

[41] Y. S. Chen, C. S. Wang, Y. J. Yang, "Combining Vibration Test with Finite Element Analysis for the Fatigue Life Estimation of PBGA Components," Microelectronics Reliability, no. 48, pp. 638-644, 2008.

[42] Q. J. Yang, H. L. J. Pang, Z. P. Wang, G. H. Lim, F. F. Yap, R. M. Lin, "Vibration Reliability Characterization of PBGA Assemblies," Microelectronics Reliability, no. 40, pp. 1097-1107, 2000.

[43] F. X. Che and J. H. L. Pang, "Vibration Reliability Test and Finite Element Analysis for Flip Chip Solder Joints," Microelectronics Reliability, no. 49, pp. 754-760, 2009.

[44] P. Lall, G. Limaye, J. Suhling, M. Murtuza, B. Palmer, W. Cooper, "Reliability of Lead-free SAC Electronics under Simultaneous Exposure to High Temperature and Vibration," 13th IEEE ITHERM Conference, 2012.

[45] J. Meng, T. Mattila, and A. Dasgupta, "Testing and Multi-scale Modeling of Drop and Impact Loading of Complex MEMS Microphone Assemblies," 13th International Conference on Thermal, Mechanical and Multi-Physics Simulation and Experiments in Microelectronics and Microsystems (EuroSimE), 2012.

[46] R. Darveaux and K. Banerji, "Constitutive Relations for Tin-Based Solder Joints," IEEE Transactions on Components, Hybrids, and Manufacturing Technology, vol. 15, no. 6, 1992.

[47] G.R. Cowper and P. S. Symonds, "Strain-hardening and Strain-rate Effects in the Impact Loading of Cantilever Beams," Technical Report No. 28, Division of Applied Mathematics, Brown University, 1957.

[48] J. Meng, T. Mattila, and A. Dasgupta, Internal study for Center of Advanced Life Cycle Engineering (CALCE), based on personal communication with Robert Darveaux, unpublished report.

[49] R. Darveaux and C. Reichman, “Mechanical Properties of Lead-Free Solders,” Proceedings of the Electronic Components and Technology Conference (ECTC), 2007.

[50] X. Niu, T. Chen, Z. Li, X. Shu, “Modeling Solder Joint Reliability of VFBGA Packages under Board Level Drop Test Based on Dynamic Constitutive Relation with Thermal Effect,” International Conference on Electronic Packaging Technology & High Density Packaging (ICEPT-HDP), 2009.

[51] K. Meier, M. Roellig, S. Wiese, K. J. Wolter, “Mechanical Behavior of Typical Lead-Free Solders at High Strain Rate Conditions,” 12th Electronics Packaging Technology Conference, 2010.

[52] M. Ernst, C. Choi and A. Dasgupta, "Computational Strategies to Minimize Transient Response During Time-Domain Analysis of Structures Under Vibratory Loading," Proceedings of the ASME InterPACK International Technical Conference and Exhibition on Packaging and Integration of Electronic and Photonic Microsystems, 2013.

[53] C. Choi and A. Dasgupta, “PoF models for Combined Vibration Fatigue and Temperature Cycling in Sac Assemblies,” Center for Advanced Life Cycle Engineering (CALCE) Consortium Meeting, 2011.

[54] K. Holdermann, G. Cuddalorepatta, and A. Dasgupta, “Dynamic Recrystallization of Sn3.0Ag0.5Cu Pb-Free Solder Alloy,” Proceedings of the ASME International Mechanical Engineering Congress and Exposition (IMECE), 2008.

[55] J. Zhao, Y. Miyashita, and Y. Mutoh, “Fatigue Crack Grwoth Behavior of 95Pb-5Sn Solder under Various Stress Ratios and Frequencies,” International Journal of Fatigue, vol 22, pp. 665-673, 2000.

[56] G. R. Johnson and W. H. Cook, “A Constitutive Model and Data for Metals Subjected to Large Strains, High Strain Rates, and High Temperatures,” Proceedings of the 7th International Symposium on Ballistics, pp. 541-547, 1983.

[57] http://www.matweb.com

[58] R. Darveaux, “Shear deformation of lead free solder joints,” Proceedings of Electronic Components and Technology Conference (ECTC), 2005.